

UNIVERSITY OF HAMBURG

MASTER'S THESIS

A Global Analysis of Mesoscale Eddy Dynamics via a Surface-Signature-Based Tracking Algorithm

Author:

NIKOLAUS KOOPMANN

Supervisor:

PROF. DR. CARSTEN

EDEN

2015/03/19

TODO: abstract

will be added last...

Contents

1	Introduction	9
1.1	Theory	9
1.1.1	Detection Methods	10
1.1.2	Eddy Drift Speeds	13
1.1.3	Eddy Horizontal Scales	14
1.2	Important Papers	16
1.2.1	Rhines 1974	16
1.2.2	Cushman-Roisin <i>et al.</i> 1990	16
1.2.3	Early Altimeter Data	17
1.2.4	Chelton <i>et al.</i> 2007; 2011	18
1.3	Satellite vs Model Data	19
2	The Algorithm	23
2.1	Step So0: Prepare Data	23
2.2	Step So1b: Find Mean Rossby Radii and Phase Speeds	24
2.3	Step So2: Calculate Geostrophic Parameters	24
2.4	Step So3: Find Contours	25
2.5	Step So4: Filter Eddies	25
2.5.1	Reshape for Filtering and Correct out of Bounds Values	26
2.5.2	Descend/Ascend Water Column and Apply Tests	26
2.6	Step So5: Track Eddies	34
2.6.1	Main Tracking Procedure	34
2.6.2	Improvements	35
2.7	Step So6: Cross Reference Old to New Indices	36
2.8	Running the Code	36
3	Results	39
3.1	MI - 7 day time-step - Aviso	42
3.2	MII - 7 day time-step - Aviso	46

3.3	MII - 7 day time-step - POP	48
3.4	MII - 7 day time-step - POP remapped to Aviso geometry	50
3.5	MII - 1 day time-step - POP	51
4	Discussion	53
4.1	Lengths of Tracks	53
4.2	Scales and the Effect of Downsampling	54
4.3	Profiles	56
4.4	Drift Speeds	56
4.5	POP-1day-MII-Southern-Ocean	57
5	Conclusion	59
5.1	POP-1day-MII-Southern-Ocean	59
5.2	things to do bla	59
Appendix A Turbulence Aspects		61
Appendix B Eddy Categories		67
Appendix C Derivations		71
Declaration of Authorship		77
Bibliography		79

<p>Definition 1: Reynolds Number Re []</p> <p>Compares advection of momentum to frictional acceleration.</p> $\text{Re} = \frac{UL}{\nu}$	<p>Definition 8: Steering Level z_S [m]</p> <p>The critical depth where the real part of the Doppler shifted phase speed $c(z_S) = c(z) - u(z) = 0$ vanishes. I.e. the depth where the Doppler shift creates a standing wave, causing the disturbances to grow in place instead of spreading in space, analogous to a <i>supersonic bang</i>.</p>
<p>Definition 2: Rossby Number Ro []</p> <p>Compares advection of momentum to Coriolis acceleration.</p> $\text{Ro} = \frac{U}{fL}$	<p>Definition 9: Sea Surface Height SSH [m]</p> <p>Vertical distance to reference geoid.</p>
<p>Definition 3: Rhines Number R_β []</p> <p>Ratio of Rhines scale to horizontal scale.</p> $R_\beta = \frac{U}{\beta L^2} = \frac{a}{L} \text{Ro}$	<p>Definition 10: gravitational acceleration g [m/s²]</p> <p>Value of surface normal component of all body forces.</p>
<p>Definition 4: Burger Number Bu []</p> <p>Ratio of relative vorticity to <i>stretching</i> vorticity.</p> $\sqrt{\text{Bu}} = \frac{NH}{fL} = \frac{L_R}{L}$	<p>Definition 11: Planetary Vorticity Ω [1/s]</p> <p>$\Omega = 4\pi/\text{day}_{fix*}$</p>
<p>Definition 5: Isoperimetric Quotient IQ []</p> <p>$\text{IQ} = A/A_c = \frac{A}{\pi r_c^2} = \frac{4\pi A}{C^2} \leq 1$. The ratio of a ring's area A to the area A_c of a circle of equal circumference C.</p>	<p>Definition 12: Surface-Normal Planetary Vorticity Component f [1/s]</p> <p>$f = f\hat{z} = \Omega \sin \phi \hat{z}$</p>
<p>Definition 6: Rhines Scale L_β [m]</p> <p>Scale at which earth's sphericity becomes relevant.</p> $L_\beta^2 = \frac{U}{\beta}$	<p>Definition 13: Change of Planetary Vorticity with Latitude β [m⁻¹s⁻¹]</p> <p>$\beta = \frac{\partial f}{\partial y} = \Omega/a \cos \phi$</p>
<p>Definition 7: Rossby Radius L_R [m]</p> <p>The <i>geostrophic wavelength</i>. $L_R = c/f$</p>	

<p>Definition 14: Okubo-Weiss Parameter $O_w \text{ [s}^{-2}\text{]}$</p> <p>Discriminant of characteristic polynomial of deformation tensor.</p> $O_w = \text{strain}_{\text{normal}}^2 + \text{strain}_{\text{shear}}^2 - \omega^2$ <p>A negative value indicates vorticity dominated motion, whereas a positive value indicates deformation. In 2 dimensions with $\nabla \cdot u = 0$:</p> $O_w = 4(u_x^2 + 4v_x u_y)$	<p>Definition 21: Mechanical Energy per mass $E_m \text{ [m}^2/\text{s}^2\text{]}$</p> <p>Sum of kinetic and potential Energy.</p>															
<p>Definition 15: dynamic eddy scale σ [m]</p> <p>Distance from eddy's center to the line of maximum orbital speed <i>i.e.</i> the zero-vorticity contour.</p>	<p>Definition 22: Reduced Gravity $g'(x, y, z) \text{ [m/s}^2\text{]}$</p> <p>In the layered model $g' = g \frac{\delta \rho}{\rho_0} = N^2 h$</p>															
<p>Definition 16: Anti-cyclone (AC)</p> <p>A vortex with sign of rotational vector opposite to Ω.</p>	<p>Definition 23: Surface/interface Displacement $\eta(x, y) \text{ [m]}$</p>															
<p>Definition 17: Cyclone (C)</p> <p>A vortex with sign of rotational vector equal to Ω.</p>	<p>Definition 24: Mean Layer thickness H [m]</p>															
<p>Definition 18: Gravity Wave Phase Speed $c \text{ [m/s}^2\text{]}$</p> <p>$c = \sqrt{g'H}$</p>	<p>Definition 25: Brunt Väisälä frequency $N \text{ [1/s]}$</p> <p>$N^2 = g / \rho_0 \frac{\partial \rho}{\partial z}$</p>															
<p>Definition 19: Buoyancy Vector B [1/s²]</p> <p>$B = -\frac{\nabla \rho \times \nabla p}{\rho^2}$</p>	<p>Definition 26: Layer Thickness/physical height of an isopycnal surface $h(x, y, \rho, t)$ [m]</p> <p>$h = H + \eta$ (in the layered model)</p>															
<p>Definition 20: Kinetic Energy per mass $E_k \text{ [m}^2/\text{s}^2\text{]}$</p>	<p>Definition 27: other physical parameters</p> <table border="0"> <tbody> <tr> <td>m</td> <td>[kg]</td> <td>mass</td> </tr> <tr> <td>ν</td> <td>[m²/s]</td> <td>Kin. Viscosity</td> </tr> <tr> <td>a</td> <td>[m]</td> <td>Earth's Radius</td> </tr> <tr> <td>ϕ</td> <td>[rad]</td> <td>Latitude</td> </tr> <tr> <td>ω</td> <td>[1/s]</td> <td>vorticity</td> </tr> </tbody> </table>	m	[kg]	mass	ν	[m ² /s]	Kin. Viscosity	a	[m]	Earth's Radius	ϕ	[rad]	Latitude	ω	[1/s]	vorticity
m	[kg]	mass														
ν	[m ² /s]	Kin. Viscosity														
a	[m]	Earth's Radius														
ϕ	[rad]	Latitude														
ω	[1/s]	vorticity														
	<p>Definition 28: Parallel Ocean Program (POP).</p> <p>Global fully non-linear 0°6', 1 d, primitive equation ocean model (Oestreicher, 2009).</p>															

Definition 29: Aviso - satellite altimetry SSH.	Definition 33: Run POP-7day-MII
Merged ERS-1/Topex-data (Forget, 2010).	7-day time-step POP with method MII.
Definition 30: Run AVI-MI	Definition 34: Run POP-1day-MII-Southern-Ocean
7-day time-step Aviso with method MI.	1-day time-step Aviso with method MII. Southern Ocean Only. Minimum Age: 30 d Contour step raised to 2 cm
Definition 31: Run AVI-MII	
7-day time-step Aviso with method MII.	
Definition 32: Run pop2avi-MII	
7-day time-step POP remapped to Aviso -geometry with method MII.	

1

Introduction

THE MAIN PURPOSE of this study is to create a computer program that is able to **detect**, **track** and **analyze** mesoscale ocean eddies via their surface signal in sea-surface-height (SSH). Due to the inherently technical character of the matter, large parts are dedicated to technicalities of the algorithm ¹. Oceanographic results are treated in the **results**- and **discussion**-chapters. This chapter discusses the physics of mesoscale geostrophic turbulence and introduces a handful of relevant historical papers. Since focus is on horizontal scales, translational speeds and the comparison of results between the **Aviso**-altimetry product and SSH-data from the **POPocean** model, sections generally focus on either of these three topics.

1.1 Theory

GEOSTROPHIC turbulence is typically characterized by rather stable, often deep reaching, more or less circular, coherent pressure anomalies that rotate fluid around in a vortex in quasi-geostrophic equilibrium ([Zhang et al., 2013](#)). These entities can persist for long periods of time in which they often travel distances on the order of hundreds of kilometers zonally. The fact that baroclinic instability leads to these vortices, instead of cascading to ever smaller scales as would be expected from chaotic turbulence, is a direct consequence of the inverse energy cascade of two-dimensional motion ² (see fig. [A.1](#)) ([Charney, 1971](#); [Brachet, 1988](#)). The atmospheric analog are storms and high-pressure systems, yet with much less difference between high- and low-pressure systems due to a smaller centrifugal force

¹ see the methods-chapter [2](#).

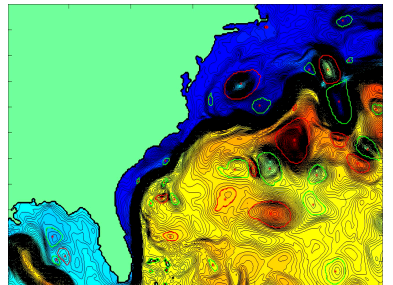


Figure 1.1: Animation snapshot of early test run. Shown is SSH with detected eddies indicated by red and green lines.

² For a discussion of this phenomenon see appendix [A](#)

i.e. smaller Rossby number (**Ro**). These quasi-geostrophic, mesoscale vortices, from here on called eddies³, are immediately visible on SSH-maps (see fig. 1.3). Yet, it is difficult to physically *define* an eddy in terms of oceanographic variables. The transition from meandering jets or other undeveloped baroclinic turbulence to a coherent vortex is not very sharp. Eddies also sometimes merge or split or collectively form rifts and valleys in SSH. Detecting them on one snapshot automatically via an algorithm is therefore not trivial. Further problems arise when the algorithm is also supposed to track each individual eddy over time. Their sheer abundance at any given time inevitably creates ambiguities as to *which is which* between time steps.

³ For a discussion of the different types of vortices in the ocean see appendix appendix B

1.1.1 Detection Methods

- One way to find an eddy in SSH-data is to simply scan for closed contours at different values for z and then subject found entities to a series of geometric tests to decide whether the contour qualifies. Only if all criteria are met is an eddy found. This method was first used by [Chelton et al. \(2011\)](#) and is certainly a relatively simple yet very effective method, at least so for satellite data. Therefore, as a starting point, this method will be adopted and should also serve as a general definition of what will be referred to as an *eddy* hereafter.

[CHELTON et al.](#) set the following threshold criteria for their algorithm:

1. The **SSH** values of all of the pixels are above (below) a given **SSH** threshold for anticyclonic (cyclonic) eddies.
 2. There are at least $[threshold]$ pixels and fewer than $[threshold]$ pixels comprising the connected region.
 3. There is at least one local maximum (minimum) of **SSH** for anticyclonic (cyclonic) eddies.
 4. The amplitude of the eddy is at least $[threshold]$.
 5. The distance between any pair of points within the connected region must be less than $[threshold]$.
- Another frequently used method to define an eddy makes use of the 2d deformation tensor ∇u .

$$\det(\lambda I - \nabla u) = 0 \quad (1.1)$$

The Sign of its squared eigenvalues indicates whether the flow-field has parabolic, vorticity dominated character, or whether deformation dominates, giving hyperbolic character. Expanding equation (1.1) yields

$$\lambda^2 - \lambda(v_y + u_x) + u_x v_y - u_y v_x = 0 \quad (1.2)$$

Assuming horizontal velocities to be much larger than vertical *i.e.* applying the small aspect-ratio assumption (Olbers *et al.*, 2012), the motion becomes 2-dimensional and the continuity equation reduces to $u_x = -v_y$. Hence

$$\lambda^2 = O_w / 4 = u_x^2 + u_y v_x \quad (1.3)$$

This is called the Okubo-Weiss-Parameter ⁴ O_w (Okubo, 1970). Its meaning is further elucidated by interpreting equation (1.3) as

$$\begin{aligned} O_w &= s_n^2 + s_s^2 - \omega^2 \\ &= (u_x - v_y)^2 + (v_x + u_y)^2 - (v_x - u_y)^2 \\ &= (u_x^2 - 2u_x v_y + v_y^2) + (v_x^2 + 2v_x u_y + u_y^2) - (v_x^2 - 2v_x u_y + u_y^2) \\ &= (u_x^2 - 2u_x v_y + v_y^2) + 4v_x u_y \\ &= (u_x^2 + 2u_x^2 + u_x^2) + 4v_x u_y \\ &= 4u_x^2 + 4v_x u_y \end{aligned} \quad (1.4)$$

where $s_{n/s}$ are the normal respective shear components of strain. Its sign thus describes the field's tendency for either vorticity- or shear-dominated motion (Isern-Fontanet, 2006). An area of large negative values of O_w indicates high enstrophy density compared to gradients of kinetic energy ⁵, thus indicating little friction paired with high momentum *i.e.* a vorticity dominated field as would be found in a coherent, angular-momentum-conserving entity. Positive values on the other hand indicate motion dominated by deformation as *e.g.* in-between two vortices of opposite sign.

⁴ see also derivation 7

⁵ Weiss, John. 1991. The dynamics of enstrophy transfer in two-dimensional hydrodynamics. *Physica*, 48, 273–294

As useful as this parameter seems, it turns out that using it to identify eddies is often not practical. Chelton *et al.* (2011) name 3 major drawbacks:

- No single threshold value for O_w is optimal for the entire World Ocean. Setting the threshold too high can result in failure to identify small eddies, while a threshold that is too low can lead to a definition

of eddies with unrealistically large areas that may encompass multiple vortices, sometimes with opposite polarities.

- O_w is highly susceptible to noise in the **SSH** field. Especially when velocities are calculated from geostrophy, the sea surface has effectively been differentiated twice and then squared, exacerbating small incontinuities in the data.
- *The third problem with the W -based method is that the interiors of eddies defined by closed contours of W do not generally coincide with closed contours of **SSH**. The misregistration of the two fields is often quite substantial.*

In summary, the O_w -method critically hinges on the necessary assumption of a smooth, purely geostrophic **SSH** topography and is therefore inferior to the approach of scanning for closed **SSH**-contours directly (as was done so by [Chelton et al.](#)) (see also [Zhang et al. \(2013\)](#)).

1.1.2 Eddy Drift Speeds

Intuitively any translative motion of a vortex should stem from an asymmetry of forces as in an imperfectly balanced gyroscope wobbling around and translating across a table. The main effects that cause a quasi-geostrophic ocean eddy to translate laterally can relatively easily be explained heuristically.

Drift Speed 1.1.2.1: Lateral Density Gradient

Consider a mean layer-thickness gradient $\frac{\partial h}{\partial x} > 0$ somewhere in the high northern latitudes and a geostrophic, positive density anomaly within that layer. In other words, a high-pressure vortex or an anti-cyclonic eddy with length scale $L \approx L_R$. Next consider a parcel of water adjacent to the eddy's northern flank of initially zero relative vorticity that is being entrained by the eddy. As the clockwise rotating eddy advects the parcel towards its eastern side, the water-column comprising said fluid will be stretched vertically as it is advected towards larger depths. In order to maintain total vorticity a small new relative-vorticity term is introduced via term C in equation (B.1c). Since the vorticity budget is dominated by the planetary component, this new term has sign of f i.e. **positive**. The opposite effect holds for a parcel advected towards the western side. Then, vortex *squeezing* leads to a new **negative** relative-vorticity term. Hence water masses on both sides of the thickness gradient acquire rotation that slowly pushes the eddy in the direction $-f \times \frac{\partial h}{\partial x}$ (in this case south). Note that since vorticity is dominated by the planetary component, the rotational sense of the eddy is irrelevant here. I.e. water columns stretched [squeezed], will always lead to new ω with sign of f [$-f$].

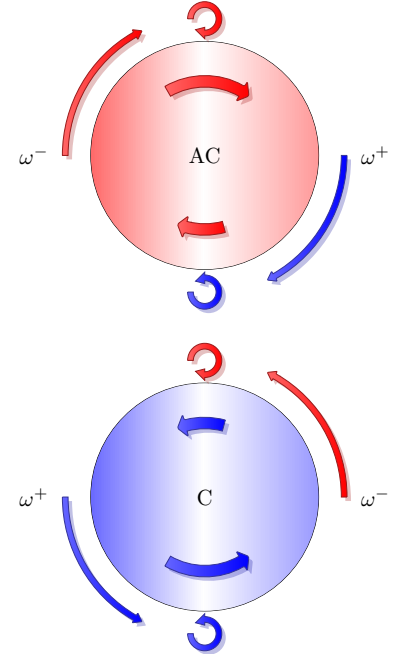


Figure 1.2: Bottom [Top]: Northern hemisphere [anti]cyclone. Blue [red] color indicates presence/production of positive [negative] relative vorticity. Advection of adjacent water masses leads to a westward drift, irrespective of the eddy's sign (see drift speed box 1.1.2.2). Inside, the discrepancy in swirl strength between north and south requires another (smaller) zonal drift term, which is eastward [westward] for [anti]cyclones.

Drift Speed 1.1.2.2: Planetary Lift

Assume now that βL be comparable or larger even than $f + \omega$ from the previous example. Then, independent of layer-thickness, all fluid adjacent to the eddy on its northern and southern flanks will be transported meridionally, thereby be tilted with respect to Ω and hence acquire relative vorticity to compensate. All fluid transported north [south] will balance the increase in planetary

vorticity with a decrease [increase] in relative vorticity. This is again independent of the eddy's sense and in this case also independent of hemisphere since $\frac{\partial f}{\partial y} = \beta > 0$ for all latitudes. The result is that small negative vortices to the northern and small positive vortices to the southern flank of eddies will push them west.

Drift Speed 1.1.2.3: Eddy-Internal β -Effect

In the later case clearly particles within the vortex undergo a change in planetary vorticity as well. Or from a different point of view, since $U \sim \nabla p/f$, and noting that the pressure gradient is the driving force here and hence fix at first approximation, particles drifting north will decelerate and those drifting south will accelerate. In order to maintain mass continuity, the center of volume will be shifted west for an anti-cyclone and east for a cyclone. Another way to look at it is to note that the only way for the discrepancy in Coriolis acceleration north and south, whilst maintaining constant eddy-relative particle speed, is to superimpose a zonal drift velocity so that net particle velocities achieve symmetric Coriolis acceleration.

(see drift speed box 1.1.2.1)

1.1.3 Eddy Horizontal Scales

THIS section discusses the motivation for exact determinations of eddy scales. That is, their horizontal extent *i.e.* their diameter or wavelength or, in the sense of turbulence.

JUST like the eddy itself, its scale is rather vague and difficult to define. What physical parameter defines the outer edge of a seamless, smooth vortex? If the eddy is detected as done by Chelton *et al.* (2011), *i.e.* closed contours of SSH, the interior of which fulfilling certain criteria, the measured perimeter may jump considerably from one time step to the next. An incremental difference in the choice of z might translate to a perimeter outlining twice the difference in area, especially when SSH gradients are small.

Another possibility is to define an amplitude first, then assume a

certain shape *e.g.* Gaussian, and then infer the radius indirectly. The obvious problem with this approach would be to properly define the amplitude.

The most physically sound method would have to be one depending on the eddy's most defining physical variable that is unambiguously determinable from SSH: the geostrophic velocities. Chelton *et al.* (2011), as with everything else, tried all methods but also conclude that the later is the most adequate one⁶.

CONSTRUED as an integral length scale of turbulence *i.e.* as the distance at which the auto-correlation of particles reaches zero (Batchelor, 1969; Eden, 2007a), the eddy-scale turns out to be of fundamental relevance for attempts to parametrize geostrophic turbulence.

GENREAL CIRCULATION MODELS ($\mathcal{O}(10^2)$ km) as they are used in *e.g.* climate forecasts are too coarse to resolve mesoscale ($\mathcal{O}(10^1)$ km) turbulence (Eden *et al.*, 2007; Eden, 2007a,b; Treguier, 1997; Ferrari & Nikurashin, 2010). Even if the Von-Neumann-condition was ignored and a refinement was desired horizontally only, a leap of one order of magnitude would effect an increase in calculation time⁷ of factor $x = 100$. The effects of the nonlinear terms therefore have to be somehow articulated in an integral sense for the large grid-boxes in the model (Fox-Kemper *et al.*, 2008; Marshall, 1981; Gent *et al.*, 1995; Killworth, 1998; Gaspar *et al.*, 1990; Griffies, 2004; Bryan *et al.*, 1999). A common approach is to assume that eddy kinetic energy $\overline{u'u'}$ and eddy potential energy $\overline{w'\rho'}$, akin to diffusive processes⁸, were proportional to the gradient of \bar{u} respective \bar{b} (down-gradient-parametrization⁹) (Olbers *et al.*, 2012; Marshall & Adcroft, 2010; Eden, 2012), which leads to the problem of finding expressions for the *turbulent diffusivities* *i.e.* the rate at which gradients are diffused by turbulence. This parameter is by no means constant, instead it can span several orders of magnitude, itself depending on the strength of turbulence-relevant gradients, and sometimes even assuming negative values (Eden & Greatbatch, 2008). Precise knowledge of the integral length scale and the physics that set it is hence vital for attempts to analyze and set values for eddy diffusivites and turbulence parameterizations in general.

TODO: [...] i took out section on eddy diffusivities

⁶ See filter 10

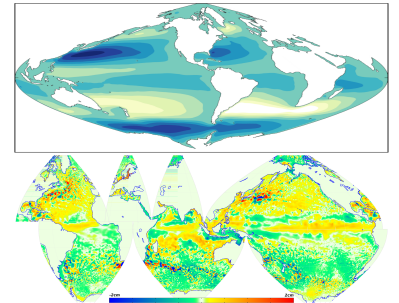


Figure 1.3: top: Stommel's equation $F_{bottom} - F_{surface} = -V\beta$ with constant eddy viscosity. bottom: POP eddy-resolving model snapshot with SSH mean of one year subtracted.

⁷ With the Moore's-Law-type exponential growth in FLOP/S of the last 22 years for supercomputers ($\lg(x) \sim 3/11a$) a factor 100 interestingly translates to only $a = 22/3 \approx 7$ years...

⁸ In analogy to Fick's first law of diffusion.

⁹ *i.e.* Reynolds averaging

1.2 Important Papers

THE following discusses a handful of selected historical papers that are concerned with either the theory of mesoscale eddies or with the detection/tracking of eddies from SSH data.

1.2.1 Waves and Turbulence on a β -Plane¹⁰

Rhines investigated the effect of the β -plane on the inverse energy cascade of quasi-2-dimensional atmospheric and oceanic turbulence. At constant f , energy should be cascaded to ever-larger scales until halted by the scale of the domain. This is clearly not the case, as no storm has ever grown to global scale. The presence of a meridional restoring force creates a critical scale beyond which the *turbulent migration of the dominant scale nearly ceases* Rossby waves are excited which would in theory eventually give way to alternating zonal jets of width $\frac{U}{\beta}$. This scale was later coined the Rhines Scale L_β .

¹⁰ Rhines, Peter B. 1974. Waves and turbulence on a beta-plane. *J. Fluid Mech.*, **69**(03), 417

1.2.2 Westward Motion of Mesoscale Eddies¹¹

Bjerknes & Holmboe (1944) already noted that the β -effect causes a mass-imbalance in planetary vortices that, if not met by an asymmetry in shape must lead to westward propagation.

Nof (1981) derived that the β -effect results in a net meridional force on the integrated mass of the vortex, which in balance with the Coriolis acceleration shoves cyclones eastward and anti-cyclones westward. They also explained how displaced water outside the eddy's perimeter causes a much stronger westward component, with the result that all eddies propagate westward irrespective of rotational sense.

The westward drift was also derived in various forms by e.g. Flierl (1984); Matsuura & Yamagata (1982).

¹¹ Cushman-Roisin, Benoit, Tang, Benyang, & Chassignet, Eric P. 1990. Westward motion of mesoscale eddies. *J. Phys.* ..., **20**(5), 758–768

THE paper by Cushman-Roisin *et al.* (1990) is particularly helpful to understand where the two components of westward drift come from. By scaling the terms in the one-layer primitive equations by their respective dimensionless numbers, integrating the interface-displacement caused by the eddy over the eddy's domain and applying mass continuity they derive for the location (X, Y) of an eddy's centroid¹²:

¹² $\langle \rangle \equiv \frac{1}{A} \int_A dA$

$$\Pi X_{tt} - Y_t = \mathbf{L}_R T \beta \langle yv \rangle + L \frac{\beta}{f} \langle y\eta v \rangle \quad (1.5)$$

$$\Pi Y_{tt} - X_t = -\mathbf{L}_R T \beta \langle yu \rangle - L \frac{\beta}{f} \langle y\eta u \rangle \quad (1.6)$$

where $\Pi = 1/f_0 T$.

Hence, independent of balance of forces the eddy's center of mass describes inertial oscillations ¹³ on the f -plane, even in the absence of β . Using geostrophic values for u and returning to dimensional variables equation (1.5) can be cast into:

$$\begin{aligned} \frac{\partial X}{\partial t} &= \frac{\beta g'}{f_0^2} \frac{\int_A H\eta \, dA + \int_A \eta^2/2 \, dA}{\int_A \eta \, dA} \\ &= \beta \left(\frac{NH}{f_0} \right)^2 + \frac{\int_A \eta^2/2 \, dA}{\int_A \eta \, dA} \quad (1.7) \\ &= \frac{\partial \omega_{long}}{\partial k} + u_{internal} \end{aligned}$$

THE first term of the RHS of equation (1.7) represents the *planetary lift* ¹⁴, which is identical to the zonal group velocity of long Rossby waves (Cushman-Roisin, 2010). The second term $u_{internal}$ represents the *eddy-internal* β -effect (see drift speed box 1.1.2.3) ¹⁵. Note that the first term is always westwards, while the second has sign of $-\eta$, i.e. westward for anti-cyclones and eastward for cyclones and that the first is always much larger than the second.

1.2.3 Early Altimeter Data

THE advent of satellite altimetry, which Walter Munk called *the most successful ocean experiment of all time* (?), finally allowed for global-scale experimental investigations of oceanic planetary phenomena on long time- and spatial scales. Among others, Matano *et al.* (1993); Cipollini *et al.* (1997); Le Traon & Minster (1993) were the first to use satellite-data to present evidence for the existence of Rossby waves and their westward-migration in accord with theory. Surprisingly all of the observations found the phase speeds to be 1 to 1.5 times larger than what theory predicted. Several theories to explain the discrepancy were presented. E.g. Killworth *et al.* (1997) argued that the discrepancy was caused by mode-2-east-west-mean-flow velocities. Interestingly it appears that hitherto, the relevant altimeter signal was

¹³ compare to harmonic oscillator

¹⁴ see drift speed box 1.1.2.2 from section 1.1.2

¹⁵ see also derivation 8

mainly associated with linear waves. Non-linearities are rarely mentioned in the papers of those years. Probably simply due to the fact that the turbulent character of much of the mesoscale variability was still obscured by the poor resolution of the first altimeter products.

1.2.4 SSH Altimeter Data¹⁶

From the beginning of satellite altimetry Chelton *et al.* have invested tremendous effort to thoroughly analyze the data in terms of Rossby waves and geostrophic turbulence. At the time of the Killworth *et al.* (1997) paper only 3 years of Topex/Poseidon data alone had been available, which led them to interpret the data mainly in terms of Rossby waves. Once the merged Aviso T/P and ERS 1/2 (Forget, 2010) was released 7 years later, Chelton *et al.* presented a new analysis that was based on an automated eddy-tracking algorithm using the geostrophic Okubo-Weiss parameter^{17,18}. For the first time satellite data was resolved sufficiently fine to unveil the dominance of *blobby structures rather than latitudinally β -refracted continuous crests and troughs* that had hitherto been assumed to characterize the large-scale SSH topography. They presented results of a refined algorithm in their 2011 paper, in which they abandoned the Okubo-Weiss concept and instead identified eddies via closed contours of SSH itself¹⁹. The improved algorithm and longer data record now allowed them to separate the non-linear eddy activity from the larger-scale Rossby waves. They find that the vast majority of extra-tropical westward propagating SSH variability does indeed consist of coherent, isolated, non-linear, mesoscale eddies that propagate about 25% slower²⁰ than the linear waves. Apart from this though they find little evidence for any dispersion in the signal, neither do they find evidence for significant meridional propagation, as should be found for Rossby waves **TODO: cite**

In agreement with Rhines & Holland (1979), they find this eddy-dominated regime to fade towards the equator, giving way to the characteristic Rossby wave profile. Almost all of their eddies propagate westwards. Those eddies that are advected eastwards by e.g. the ACC show significantly shorter life-times than those that are not. For more detail on their results and a discussion of the limitations of eddy-tracking via satellites (see section 1.3).

¹⁶ Chelton, Dudley B., Schlax, Michael G., Samelson, Roger M., & de Szoeke, Roland a. 2007. Global observations of large oceanic eddies. *Geophys. Res. Lett.*, 34(15), L15606; and Chelton, Dudley B., Schlax, Michael G., & Samelson, Roger M. 2011. Global observations of nonlinear mesoscale eddies. *Prog. Oceanogr.*, 91(2), 167–216

¹⁷ see section 1.1.1

¹⁸ see Derivation derivation 7

¹⁹ note that geostrophic O_W is a second derivative of SSH and thus exacerbates noise in the SSH data.

²⁰ pointing to dispersion.

TODO: i took out...

- **Eden 2006; Eden et al. 2007; Eden & Greatbatch 2008; Gent et al. 1995; Larichev & Held 1995; Eden 2007a, 2011, 2012; Vollmer & Eden 2013; Tulloch et al. 2009; Gent & Mcwilliams 1990; Gent et al. 1995; Larichev & Held 1995; Scott & Wang 2005**

1.3 Satellite vs Model Data

1.3.0.0.1 The latest Aviso SSH data from satellites features impressive accuracy, constancy and resolutions in both space and time. This is achieved by collecting all of the data from all of the altimeter-equipped satellites available at any given moment for any given coordinate. This conglomerate of highly inhomogeneous data is then subjected to state-of-the-art interpolation methods to produce a spatially and temporally coherent product. One satellite alone is not sufficient to adequately resolve mesoscale variability globally.

E.g. the Topex/Poseidon satellite had a ground repeat track orbit of 10 days and circled the earth in 112 minutes or ≈ 13 times a day with a swath width of 5 km. Hence it drew ~ 26 5-km-wide stripes onto the globe every day. The orbit's precession is such that this pattern is then repeated after 10 days, which means that at the equator only $10 \times 26 \times 5 = 1300$ km of the $2\pi \times 6371 = 40000$ km get covered, *i.e.* 3.25%. At every 10d time-step, on average, effectively $(40000 - 1300)/26 = 1490$ km are left blank in-between swaths on the equator. This is why, no matter how fine the resolution within the swath at one moment in time may be, the spatial resolution is so coarse.

The merged ERS-1/Topex-data as used by Chelton et al. (2011) has a time step of 7 days. Assuming eddy drift speeds of $u_e = \mathcal{O}(10^{-1})$ m/s implies a distance traveled per time step of $L_{\delta t} \approx 60$ km. Chelton et al. estimate their effective spatial resolution as $\delta x \approx 40$ km. Eddies of smaller scale are not resolved.

TRACKING a single eddy from one time-step to the next is complicated by the sheer abundance of eddies at any given point in time and the fact that eddy activity is usually concentrated into regions of strong geostrophic turbulence.

	POP	merged T/P - ERS-1
dx	7km – 11km	1/3° (≈ 40 km after filtering)
dt	1d	7d
$\log_{10} 2$ filter cutoff	–	2° by 2°
z-levels	4 ²	1
variables	SSH, S, T, u/v/w, tracers etc	SSH
pot. interpolation artifacts	–	yes
reality	no	yes

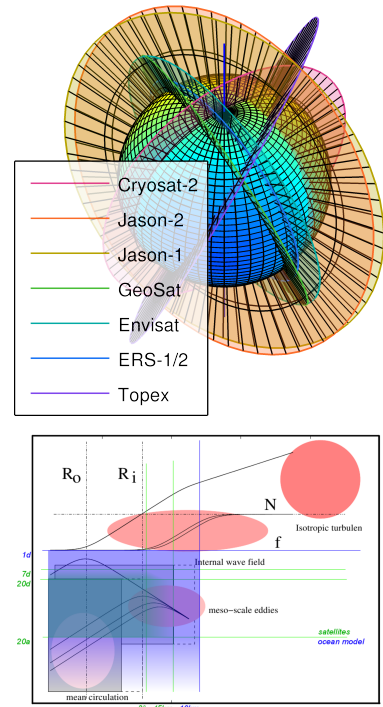
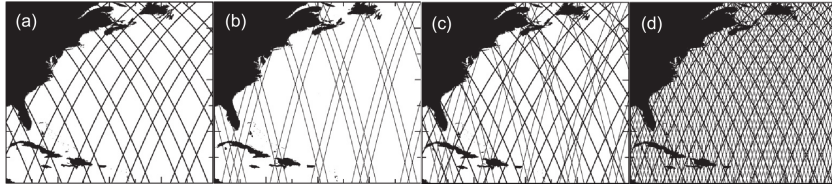
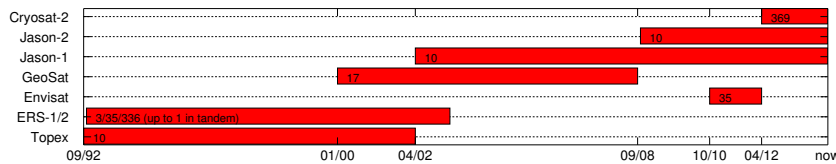


Figure 1.4: Resolutions for model vs satellite. Modified version from Olbers et al. (2012).



THE ambiguities in matching the eddies from the old time-step to those of the new one might cause aliasing effects in the final statistics.



THE translational speeds ²¹ of eddies are not really the problem here, as they usually drift slow enough to not cover more than 1 grid node per 7 day time step. The issue are those areas where eddies are born, die and merge. According to [Smith & Marshall \(2009\)](#), instabilities within the ACC grow at rates of up to $1/(2\text{days})$, which means that at one time-step up to 3 eddies have emerged and equally many died for every eddy identified within such region. The ground-repeat-frequency of a satellite can of course not be set arbitrarily. Especially when the satellite is desired to cover as far north and south as possible, whilst still being subjected to just the right torque from the earth's variable gravitational field to precess at preferably a sun-synchronous frequency *i.e.* $360^\circ/\text{year}$ (?). Neither can the satellite's altitude be chosen arbitrarily. If too low the oblateness of the earth creates too much eccentricity in the orbit that can no longer be *frozen*²². Another problem could be potential inhomogeneity in the merged data in time dimension, since data of old and current missions are lumped together into one product. This is why [Chelton et al. \(2011\)](#) opted against the finest resolution available and instead went for a product that had the most satellites merged in unison for the longest period of time.

Figure 1.5: The ground track patterns for the 10-day repeat orbit of T/P and its successors Jason-1 and Jason-2 (thick lines) and the 35-day repeat orbit of ERS-1 and its successors ERS-2 and Envisat (thin lines). (a) The ground tracks of the 10-day orbit during a representative 7-day period; (b) The ground tracks of the 35-day orbit during the same representative 7-day period; (c) The combined ground tracks of the 10-day orbit and the 35-day orbit during the 7-day period; and (d) The combined ground tracks of the 10-day orbit and the 35-day orbit during the full 35 days of the 35-day orbit. (sic) ([Chelton et al., 2011](#)) Figure 1.6: Length of mission. Numbers are orbit-period in days.

²¹ $\mathcal{O}(10^1)\text{km/day}$

²² minimizing undulating signals in altitude by choosing the right initial values (?)

THE surface velocities inferred from altimetry are the geostrophic components only, which should suffice to *e.g.* determine the non-linearity and kinetic energy of an eddy for almost all regions, but less so for *e.g.* the western boundary currents.

Box 1: Horizontal Resolution

Assume $Bu = 1$, so that $L = NH/f$ and $NH = a/10d$ (corresponds to $L(\phi = 30^\circ) = 100\text{km}$), a model resolution of $1^\circ/\mu$ and that the eddy diameter was twice the Rossby radius. Then, how many grid notes ξ fit into one eddy as a function of latitude?

$$\begin{aligned} \xi \frac{a \cos \phi}{\mu 2\pi} &= \frac{2NH}{f} = \frac{2NH1d}{4\pi \sin(\phi)} \\ \xi &= \frac{2\mu}{10 \sin(2\phi)} \end{aligned} \quad (1.8)$$

In this flat-bottom, constant ρ_z , Mercator-gridded model the worst eddy-resolution is interestingly at mid-latitude (see fig. 1.7).

THE finer resolution of the POP data in space and time should certainly yield more precise results. It must be kept in mind though that by using the model data, what one analyses is of course just that - a *model*. Baroclinic geostrophic space/time scales depend crucially on *e.g.* the vertical density structure (see section 1.2.2, Charney (1971)), which is resolved only poorly in the model. A useful comparison among satellite/model results should hence be tricky.

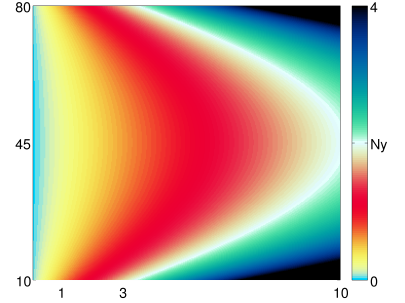


Figure 1.7: $\xi(\phi, \mu)$. $Ny \equiv 2$ i.e. the Nyquist frequency.

2

The Algorithm

TODO: resort some stuff to intro/discussion..

This section walks through the algorithm step by step, so as to explain which methods are used and how they are implemented. The idea is that the code from step `S00...` on can only accept one particular structure of data. In earlier versions the approach was to write code that would adapt to different types of data automatically. All of this extra adaptivity turned out to visually and structurally clog the code more than it did offer much of a benefit. The concept was therefor reversed. Input SSH-data needs to be altered to required format. Yet, there should be no need to adapt any of the later steps in any way. All input parameters are to be set in `INPUT.m` and `INPUTX.m`.

2.1 Step S00: Prepare Data

```
function S00_prep_data
```

Before the actual eddy detection and tracking is performed, SSH-, latitude- and longitude-data is extracted from the given data at desired geo-coordinate bounds and saved as structures in the form needed by the next step (S01). This step also builts the file `window.mat` via `GetWindow3` which saves geometric information about the input and output data as well as a cross-referencing index-matrix which is used to reshape all *cuts* to the user-defined geo-coordinate-geometry. The code can handle geo-coordinate input that crosses the longitudinal seam of the input data. E.g. say the input data came in matrices that start and end on some (not necessarily strictly meridional) line straight across the Pacific and it is the Pacific only that is to be analyzed for eddies, the output maps are stitched accordingly. In the zonally continous case *i.e.* the full-longitude case,

an *overlap* in x-direction across the *seam*-meridian of the chosen map is included so that contours across the seam can be detected and tracked across it. One effect is that eddies in proximity to the seam can get detected twice at both zonal ends of the maps. The surplus double-eddies get filtered out in `S05_track_eddies`.

2.2 Step S01b: Find Mean Rossby Radii and Phase Speeds

```
function S01b_BruntVaisRossby
```

This function...

- – ...calculates the pressure $P(z, \phi)$ in order to...
 - ...calculate the Brunt-Väisälä-Frequency according to $N^2(S, T, P, \phi) = -\frac{g(\phi)}{P} \frac{\partial \rho(S, T, P)}{\partial z}$ in order to...
- – ...integrate the Rossby-Radius $L_R = \frac{1}{\pi f} \int_H N dz$ and ...
 - apply the long-Rossby-Wave dispersion relation to found L_R to estimate Rossby-Wave phase-speeds $c = -\frac{\beta}{k^2 + (1/L_r)^2} \approx -\beta L_R^2$

The 3-dimensional matrices (S and T) are cut zonally into slices which then get distributed to the threads. This allows for direct matrix operations for all calculations which would otherwise cause memory problems due to the immense sizes of the 3d-data¹.

¹ E.g. the POP data has dimensions $42 \times 3600 \times 1800$.

2.3 Step S02: Calculate Geostrophic Parameters

```
function S02_infer_fields
```

This step reads the cut `SSH` data from `S00_prep_data` to perform 2 steps:

1. Calculate a mean over time of $SSH(y, x)$.
2. • use one of the files' geo-information to determine f , β and g .
 - calculate geostrophic fields from `SSH` gradients.
 - calculate deformation fields (vorticity, divergence, stretch and shear) via the fields supplied by the last step.
 - calculate O_w .
 - Subtract the mean from step 1 from each $SSH(t)$ to filter out persistent SSH-gradients e.g. across the Gulf-Stream.

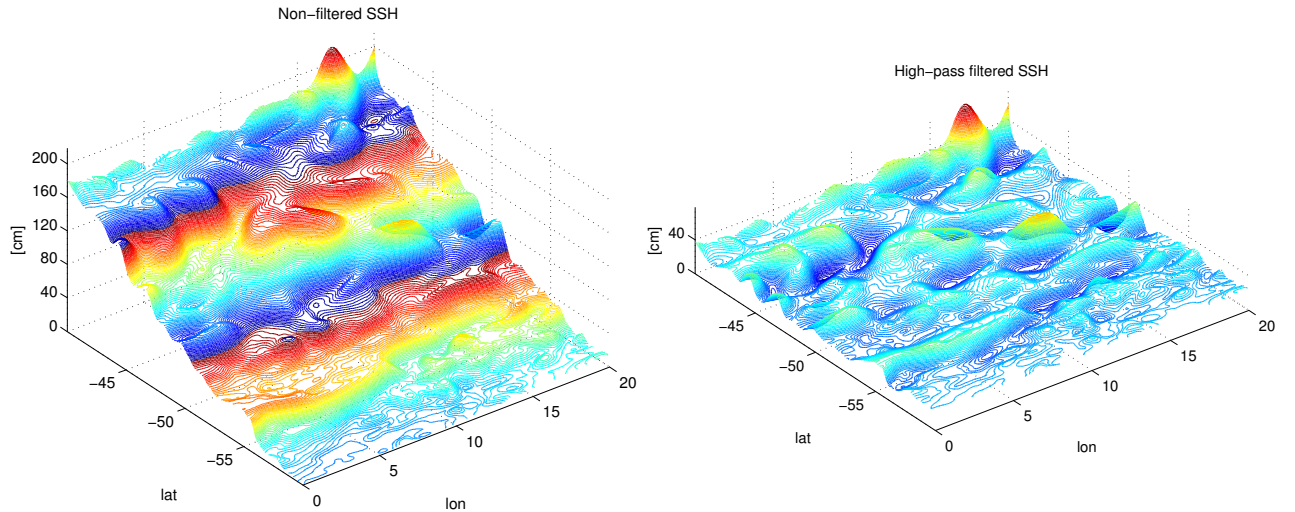


Figure 2.1: SSH with mean over time subtracted.

2.4 Step S03: Find Contours

```
function S03_contours
```

The sole purpose of this step is to apply MATLAB's `contourc.m` function to the `SSH` data. It simply saves one file per time-step with all contour indices appended into one vector². The contour intervals are determined by the user defined increment and range from the minimum- to the maximum of given `SSH` data.

The function `initialise.m`, which is called at the very beginning of every step, here has the purpose of rechecking the *cuts* for consistency and correcting the time-steps accordingly (*i.e.* when files are missing). `initialise.m` also distributes the files to the threads *i.e.* parallelization is in time dimension.

² see the MATLAB documentation.

2.5 Step S04: Filter Eddies

```
function S04_filter_eddies
```

Since indices of all possible contour lines at chosen levels are available at this point, it is now time to subject each and every contour to a myriad of tests to decide whether it qualifies for the outline of an eddy as defined by the user input threshold parameters.

2.5.1 Reshape for Filtering and Correct out of Bounds Values

```
function eddies2struct
function CleanEddies
```

In the first step the potential eddies are transformed to a more sensible format, that is, a structure `Eddies` of size `EddyCount`. The struct has fields for level, number of vertices, exact *i.e.* interpolated coordinates and rounded integer coordinates.

The interpolation of `contourc.m` sometimes creates indices that are either smaller than 0.5 or larger than ³ $N + 0.5$ for contours that lie along a boundary. After rounding, this seldomly leads to indices of either 0 or $N + 1$. These values get set to 1 and N respectively in this step.

³ where N is the domain size

2.5.2 Descend/Ascend Water Column and Apply Tests

```
function walkThroughContsVertically
```

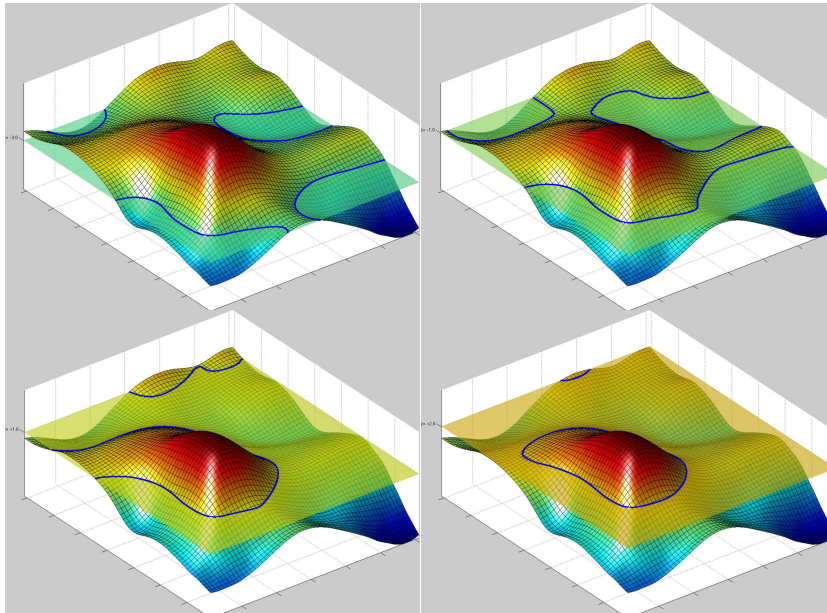


Figure 2.2: The algorithm approaches the appropriate vertical level incrementally.

The concept of this step is a direct adaption of the algorithm described by [Chelton et al. \(2011\)](#). It is split into two steps, one for anti-cyclones and one for cyclones. Consider *e.g.* the anti-cyclone situation. Since all geostrophic anti-cyclones are regions of relative

high pressure, all **ACs** effect an elevated **SSH** *i.e.* a *hill*. The algorithm ascends the full range of **SSH** levels where contours were found. Consider an approximately Gaussian shaped **AC** that has a peak **SSH** of say 5 increments larger than the average surrounding waters. As the algorithm approaches the sea surface from below, it will eventually run into contours that are closed onto themselves and that encompass the **AC**. At first these contours might be very large and describe not only one but several **ACs** and likely also cyclones, but as the algorithm continues upwards found contour will get increasingly circular, describing some outer *edge* of the **AC**. Once the contour and its interior pass all of the tests, the algorithm will decide that an **AC** was found and write it and all its parameters to disk. The **AC**'s region *i.e.* the interior of the contour will be flagged from here on. Hence any inner contour further up the water column will not pass the tests. Once all **ACs** are found for a given time-step, the **SSH** flags get reset and the entire procedure is repeated, only this time *descending* the **SSH**-range to find cyclones. The tests for cyclones and anti-cyclones are therefor identical except for a factor -1 where applicable. In the following the most important steps of the analysis are outlined.

TODO: format filters

Contour filter 1 NaN-Check Contour

```
function CR_RimNan
```

The first and most efficient test is to check whether indices of the contour are already flagged. Contours within an already found eddy get thereby rejected immediately.

Contour filter 2 Closed Ring

```
function CR_ClosedRing
```

Contours that do not close onto themselves are obviously not eligible for further testing.

Contour filter 3 Sub-Window

```
function get_window_limits, EddyCut_init
```

For further analysis a sub-domain around the eddy is cut out of the **SSH** data. These functions determine the indices of that window and subtract the resultant offset for the contour indices.

Contour filter 4 Logical Mask of Eddy Interiour

```
function EddyCut_mask
```

Basically this function creates a **flood-fill** logical mask of the eddy-

interior. This is by far the most calculation-intensive part of the whole filtering procedure. A lot more time was wasted on attempting to solve this problem more efficiently than time could have been saved would said attempts have been successful. The current solution is basically just MATLAB's `imfill.m`, which was also used in the very first version of 09/2013. EDIT: `imfill.m` was replaced by using `inpoly.m` to determine which indices lie within the contour-polygon. This method seems to be more exact at determining whether the inside-part of one grid cell (with respect to the smooth, spline-interpolated contour) is larger than the outside part or not.

Contour filter 5 Sense

```
function CR_sense
```

All of the interior SSH values must lie either above or below current contour level, depending on whether anti-cyclones or cyclones are sought.

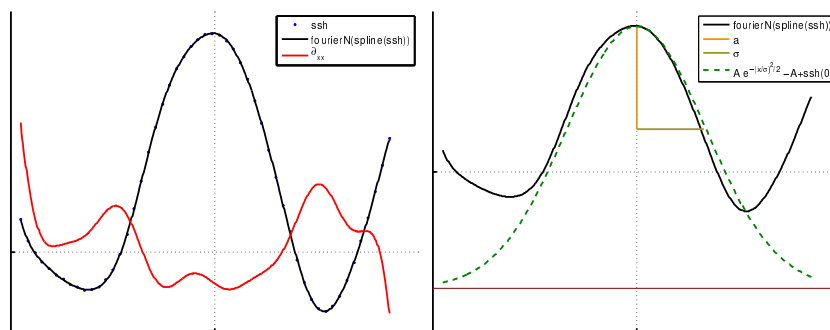


Figure 2.3: Left: Fourier-fit of an eddy from POP SSH-data and the 2nd differential thereof. Right: Theoretical Gauss shape built from the resulting *standard-deviation* i.e. σ and amplitude.

Contour filter 6 Area

```
function getArea
```

The main goal here is to determine the area encompassed by the interpolated coordinates of the contour. It does so via MATLAB's `polyarea` function. This area is not related to the scale σ that is determined in filter 12. It is however the relevant scale for the determination of the isoperimetric quotient in filter 8.

If the respective switch is turned on, this function also checks that the area of found contour does not surpass a given threshold which in turn is a function of L_R . Since L_R gets very small in high latitudes a lower bound on the L_R used here should be set as well. This is especially important for the southern ocean where L_R gets very small

while the strong mesoscale turbulence of the Antarctic circumpolar current results in an abundance of relatively large eddies as far south as 60°S and beyond.

Contour filter 7 Circumference

`function EddyCircumference`

Circumference *e.g.* line-length described by the contour. This is the other parameter needed for filter 8. This is however neither related to the actual eddy scale determined in filter 12.

Contour filter 8 Shape

`function CR_Shape`

This is the crucial part of deciding whether the object is *round enough*. A perfect vortex with $\frac{\partial u}{\partial y} = -\frac{\partial v}{\partial x}$ is necessarily a circle. The problem is that eddies get formed, die, merge, run into obstacles, get asymmetrically advected etc. To successfully track them it is therefore necessary to allow less circle-like shapes whilst still avoiding to *e.g.* count 2 semi-merged eddies as one. This is achieved by calculating the **isoperimetric quotient**, defined as the ratio of a ring's area to the area of a circle with equal circumference. Chelton *et al.* (2011) use a similar method. They require:

The distance between any pair of points within the connected region must be less than a specified maximum (Chelton *et al.*, 2011).

While this method clearly avoids overly elongated shapes it allows for stronger deformation within its distance bounds.

Contour filter 9 Amplitude

`function CR_AmpPeak`

This function determines the amplitude *i.e.* the maximum of the absolute difference between **SSH** and current contour level and the position thereof as well as the amplitude relative to the mean **SSH** value of the eddy interior as done by Chelton *et al.* (2011). The amplitude is then tested against the user-given threshold. The function also creates a matrix with current contour level shifted to zero and all values outside of the eddy set to zero as well.

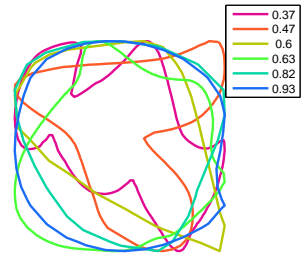


Figure 2.4: Different values of the isoperimetric quotient.

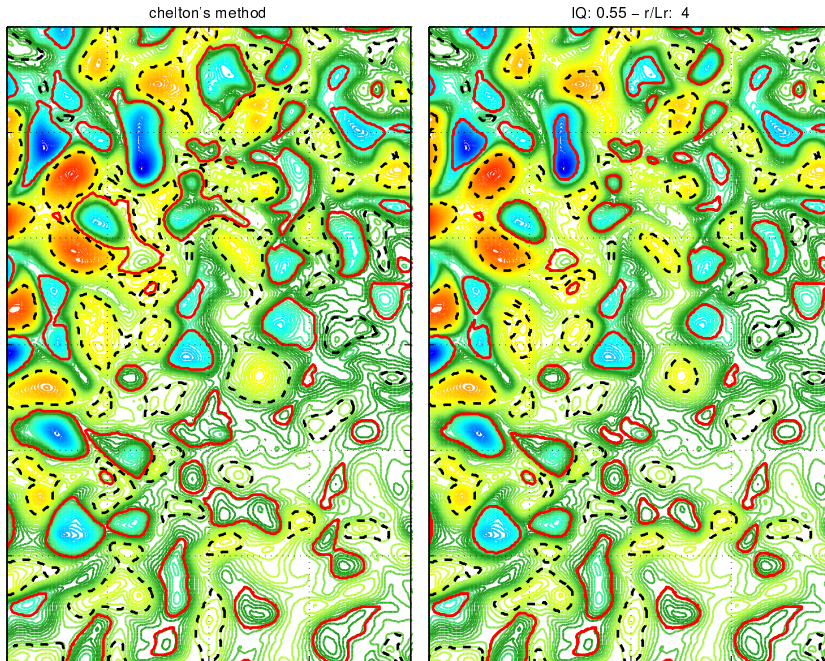


Figure 2.5: Left: The Chelton-method expects to detect eddies at their base and is rather tolerant with respect to the shape of found contour. The IQ-method aims more at detecting single round vortices without expecting found contour to be necessarily related to any howsoever-defined outer edge of the eddy.

Contour filter to Chelton's Scales

```
function cheltStuff
Chelton et al. (2011) introduced 4 different eddy-scales.
```

1. The effective scale L_{eff} as the radius of a circle with its area equal to that enclosed by the contour.
2. The scale L_e as the radius at $z = e^{-1}a$ with a as the amplitude with reference to the original contour and the z -axis zero-shifted to that contour. In other words the effective scale of the contour that is calculated at $1/e$ of the original amplitude.
3. The scale $L = L_e/\sqrt{2}$.
4. The scale L_s which is a direct estimate based on the contour of SSH within the eddy interior around which the average geostrophic speed is maximum (Chelton et al., 2011). It is hence conceptually the same as σ . This scale was not calculated here, as I could not think of an efficient, simple way to estimate the area bounded by maximum geostrophic

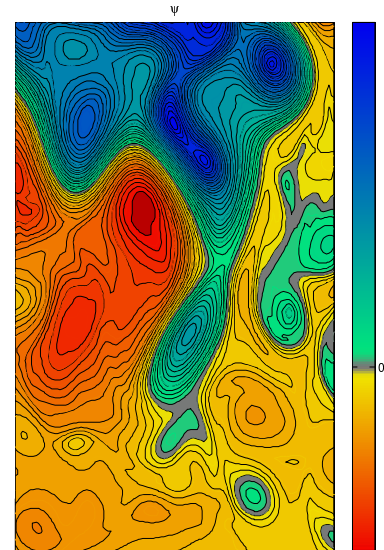


Figure 2.6: Stream function of a meandering jet shedding off a vortex. The line of strongest gradient i.e. fastest geostrophic speed later becomes the zero-vorticity-line at a theoretical distance σ from the center (Offset of Ψ is chosen arbitrarily).

speed *i.e.* the zero-vorticity contour. To understand why this would be difficult to achieve see also filter 12, ????, and section 1.3.

Contour filter 11 Profiles

`function EddyProfiles`

This step

- saves the meridional and zonal profiles of SSH, U and V through the eddy's peak, spanning the entire sub-domain as described in filter 4.
- creates spline functions from the ssh-profiles and uses them to interpolate the profiles onto 100-piece equi-distant coordinate vectors to build smooth interpolated versions of ssh-profiles in both directions.
- in turn uses the splined data to create smooth 4-term Fourier series functions for the profiles.

Contour filter 12 Dynamic Scale (σ)

`function EddyRadiusFromUV`

The contour line that is being used to detect the eddy is not necessarily a good measure of the eddy's *scale* *i.e.* it doesn't necessarily represent the eddy's outline very well. This becomes obvious when the area, as inferred by filter 6, is plotted over time for an already successfully tracked eddy. The result is not a smooth curve at all. This is so because at different time steps the eddy usually gets detected at different contour levels. Since its surrounding changes continuously and since the eddy complies with the testing-criteria the better the closer the algorithm gets to the eddy's peak value, the determined area of the contour jumps considerably between time steps. This is especially so for large flat eddies with amplitudes on the order of 1cm. If the contour increment is on that scale as well, the difference in contour-area between two time steps easily surpasses 100% and more. Since there is no definition for the *edge* of an eddy, it is defined here as the ellipse resulting from the meridional [zonal] diameters that are the distances between the first local extrema of orbital velocity (one negative, one positive) away from the eddy's peak in y- [x-] direction ⁴. In the case of a meandering jet with a maximum flow speed at its center, that is shedding off an eddy, this scale corresponds to half the distance between two opposing center-points of the meander. It is



Figure 2.7: Zonal x- and z-normalized cyclone-profiles (early data ~ '13/12).

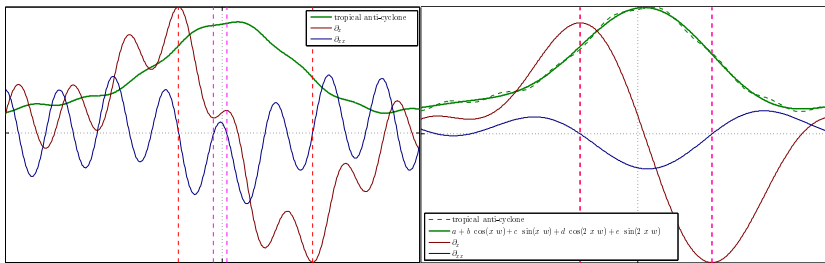
⁴ The velocities are calculated from the gradients of 4th-order Fourier fits to the SSH profile in respective direction (see filter 11).

also the distance at which a change in vorticity-polarity occurs and is thus assumed to be the most plausible dividing line between vortices.

Trying to determine the location where this sign change in vorticity occurs in the profiles turns out to be very tricky. What we seek are local extrema of the geostrophic speeds *i.e.* of the ssh-gradients h_x . In a perfect Gaussian-shaped eddy, these would simply correspond to the first local extrema of h_x away from the peak. In *reality* the eddies can be very wobbly with numerous local maxima and minima in the gradients of their flanks. One could argue, that it must be the largest extrema, as it is the highest geostrophic speeds that are sought. In practice⁵ multiple superimposed signals of different scales often create very strong gradients locally. But the main issue here is that one weak eddy adjacent to one strong eddy also has the stronger gradients of the stronger one within its domain so that simply looking for the fastest flow speeds along the profiles is insufficient. It is also not possible to restrict the cut domain to the extent of a single eddy only, because at the time when the domain is selected, we do not know yet whether the detection algorithm *took bait* at the eddy's base or later close to the tip.

The best method thus far seems to be to use the Fourier-series functions from filter 11 to determine the first extrema away from the eddy's peak (see fig. 2.8). The Fourier order was chosen to be 4 by trial and error. The effect is that small-scale low-amplitude noise is avoided, allowing for more reliable determinations of $\nabla^2 h_{\text{fourier}} = 0$.

Once the zero crossings in all 4 directions are found, their mean is taken as the eddy's scale (σ).



⁵ especially for the high-resolution model data.

Figure 2.8: A flat wobbly low-latitude eddy resulting in multiple zero-crossings of its ∇^2 . The problem is addressed by differentiating the profile's Fourier-Series fit instead.

Contour filter 13 Dynamic Amplitude

```
function EddyAmp2Ellipse
```

As mentioned above, the contour that helps to detect the eddy is not representative of its extent. This is also true for the z-direction, for the

same reasons. This function therefor takes an SSH-mean at indices of the ellipse created by the determined zonal and meridional *dynamical* diameters, and uses this as the basal value to determine a *dynamic* amplitude.

Contour filter 14 Center of Volume (CoV)

```
function CenterOfVolume
```

Instead of using the geo-position of the eddy's peak in the tracking procedure, it was decided to instead use the center of the volume created by the basal shifted matrix from filter 9 *i.e. the center of volume of the dome (resp. valley) created by capping off the eddy at the contour level*. This method was chosen because from looking at animations of the tracking procedure it became apparent that, still using peaks as reference points, the eddy sometimes jumped considerably from one time step to the next if two local maxima existed within the eddy. E.g. in one time-step local maximum A might be just a little bit larger than local maximum B and one time-step later a slight shift of mass pushes local maximum B in pole position, creating a substantial jump in the eddy-identifying geo-position hence complicating the tracking procedure.

Contour filter 15 Geo Projection

```
function ProjectedLocations
```

An optional threshold on the distance an eddy is allowed to travel over one time-step is implemented in the tracking algorithm in section 2.5. This is a direct adaptation of the ellipse-based constraint described by Chelton *et al.* (2011). The maximum distance in western direction traveled by the eddy within one time-step is limited according to $x_{west} = \alpha c \delta t$ with c as the local long-Rossby-wave phase-speed and

e.g. $\alpha = 1.75$. In eastern direction the maximum is fixed to a value of e.g. $x_{east} = 150\text{km}$. This value is also used to put a lower bound on x_{west} and for half the minor axis (y -direction) of the resultant ellipse.

This function builds a mask of eligible geo-coordinates with respect to the next time-step.

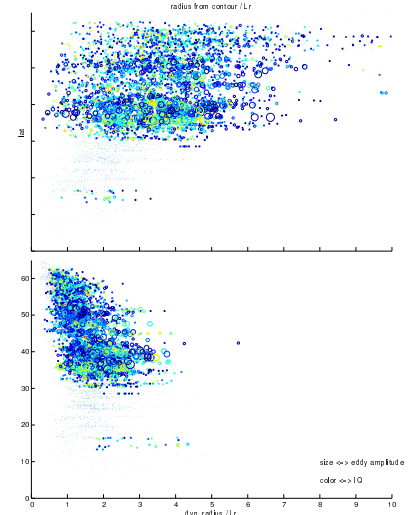


Figure 2.9: Eddies in the North-Atlantic. Y-axis: latitude. X-axis top: ratio of radius of circle with equal area to that of found contour to local Rossby-radius. X-axis bottom: ratio of σ to local Rossby-radius. Color-axis: Isoperimetric Quotient. Size: amplitude. The bottom plot suggests that a ratio of say 4 for σ/L_R should be a reasonable threshold. Same graph for the Southern Ocean looks very different though (not shown here), in that said ratio often exceeds ratios as high as 10 and larger in the far south where L_R becomes very small. This problem was addressed by prescribing a minimum value $L_R = 20\text{km}$ for the calculation of the scale-theshold.

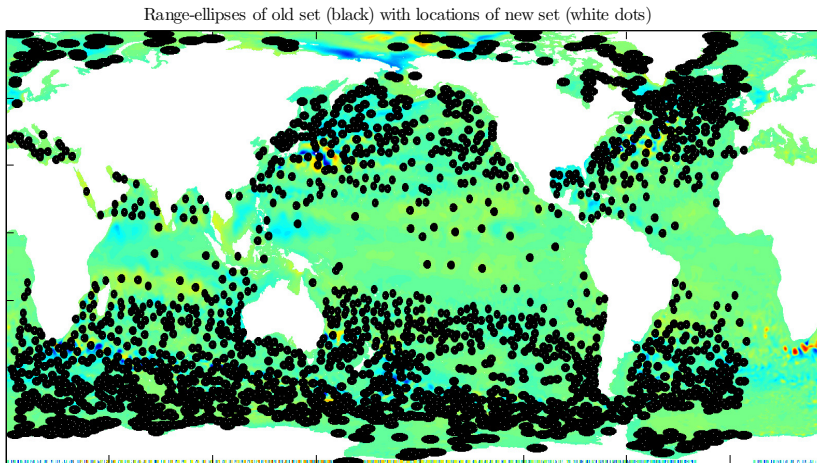


Figure 2.10: Among the saved meta-information for each eddy are also the indices describing the ellipse that defines the eddy's allowed locations for the next time-step.

2.6 Step S05: Track Eddies

S05_track_eddies

2.6.1 Main Tracking Procedure

Due to the relatively fine temporal resolution (daily) of the model data, the tracking procedure for this case turns out to be much simpler than the one described by Chelton *et al.* (2007). There is almost no need to project the new position of an eddy, as it generally does not travel further than its own scale in one day. This means that one eddy can usually⁶ be tracked unambiguously from one time step to the next as long both time-steps agree on which eddy from the other time-step is located the least distance away. The algorithm therefore simply builds an arc-length-distance matrix between all old and all new eddies and then determines the minima of that matrix in both directions *i.e.* one array for the new with respect to the old, and one for the old with respect to the new set. This leads to the following possible situations:

- Old and new agree on a pair. I.e. old eddy O_a has a closest neighbour N_a in the new set and N_a agrees that O_a is the closest eddy from the old set. Hence the eddy is tracked. N_a is O_a at a later time.
- N_a claims O_a to be the closest, but N_b makes the same claim.

⁶ The only exception being the situation when one eddy fades and another emerges simultaneously and in sufficient proximity.

I.e. two eddies from the new set claim one eddy from the old set to be the closest. In this situation the closer one is decided to be the old one at a later time-step and the other one must be a newly formed eddy.

- At this point all new eddies are either allocated to their respective old eddies or assumed to be *newly born*. The only eddies that have not been taken care of are those from the old set, that *lost* ambiguity claims to another old eddy, that was closer to the same claimed new eddy. I.e. there is no respective new eddy available which must mean that the eddy just *died*. In this case the entire track with all the information for each time step is archived as long as the track-length meets the threshold criterium. If it doesn't, the track is abandoned.

2.6.2 Improvements

The former is the core of the tracking algorithm. It is almost sufficient by itself as long as the temporal resolution is fine enough. The larger the time-step, the more ambiguities arise, which are attempted to be mitigated by flagging elements of the distance matrix not meeting certain thresholds:

- `function checkDynamicIdentity`

Consider the ambiguous case when there are two new eddies N_a and N_b in sufficient proximity to old eddy O_a . Let's assume O_a is a relatively solid eddy of rel. large scale with a steep slope i.e. large amplitude and that N_a is merely a subtle blob of an eddy whilst N_b is somewhat similar to O_a but with only half the amplitude. The situation then is clear: N_b is the, apparently slowly dying, O_a at a later time, while N_a could either be a newly formed eddy, an old eddy with its respective representation in the old set something other than O_a , or even just temporary coincidental noise not representative of any significant mesoscale vortex at all. This interpretation should hold even when O_a sat right between the other two, thereby being much closer to O_a than N_b was.

The purpose of this step is to make such decisions. It does so by comparing the *dynamic* versions of amplitude and scale (*ampToElliipse* and σ) between the time-steps. If either ratio from new to old⁷ surpasses a given threshold, the pair is flagged as non-eligible. It is important to use the *dynamic* parameters rather than those

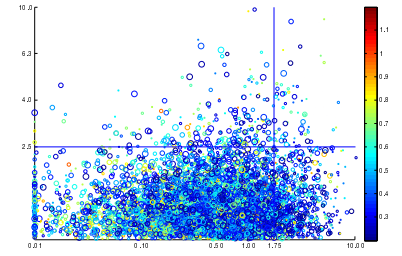


Figure 2.11: Each circle represents one eddy in the new time step. Y-axis: Maximum ratio to closest eddy in old set of either amplitude or σ , where 1 means *identical* and 2 means factor 2 difference. The threshold used for the final runs was 2. X-axis: Ratio of distance to closest eddy from old set divided by δt to local long-Rossby-wave phase-speed. Color-axis: Isoperimetric Quotient. Radius of circles: ratio of σ to local Rossby-radius. All eddies with said ratio larger than 10 are omitted. Note the obvious inverse correlation of scale to IQ, suggesting that all large *eddies* likely represent more than one vortex.

⁷ In order to compare in both directions equally: $\exp(|\log(v_n/v_o)|)$ where v is either amplitude or scale.

stemming from the contour line, because as mentioned in filter 12, the contour line itself and the eddy's geometric *character* are hardly correlated at all. One eddy can get detected at different z-levels from one time-step to the next, resulting in completely different amplitudes, scales and shapes with respect to the contour.

The initial idea was, by assuming Gaussian shapes, to construct a single dimensionless number representing an eddy's geometrical character built upon the contour-related amplitude- and scale values only. Since we have no information about the vertical position of a given contour with respect to assumed Gauss bell, this problem turned out to be intrinsically under-determined and hence useless. The method eventually used, which checks amplitude and scale separately is again very similar to that described by Chelton *et al.* (see Box box 2).

- `function nanOutOfBounds`

This is the second half of the prognostic procedure described in section 2.6. It simply flags all pairs of the distance matrix for which the index representing the *new* eddy's geographic location is not among the set of indices describing the ellipse⁸ around respective *old* eddy.

- `function checkAmpAreaBounds`

This is the direct adaptation of Chelton *et al.*'s description of how to test for sufficient similarity of amplitude and area between time steps.

⁸ see figure fig. 2.10.

2.7 Step S06: Cross Reference Old to New Indices

`function S05_init_output_maps`

The output Mercator-maps usually have different geometry from the input maps'. This step allocates all grid nodes of the input data to their respective nodes in the output map. Each output cell will then represent a mean of all input-nodes falling into that quadrilateral.

2.8 Running the Code

The separate steps can be run all at once (`Sall.m`) or one by one, as long as they are started consecutively in the order indicated by their name (`S00..`, then `S01..` etc.). `S01b` is not necessary though. Each step either creates its own output files or extends old ones, which

are then read by the next step. All output data is saved in the user given root-path. This concept uses quite a lot of disk space and is also slowed substantially by all the reading and writing procedures. The benefit is that debugging becomes much easier. If the code fails at some step, at least all the calculations up to that step are dealt with and do not need to be re-run. The concept also makes it easier to extend the code by further add-ons.

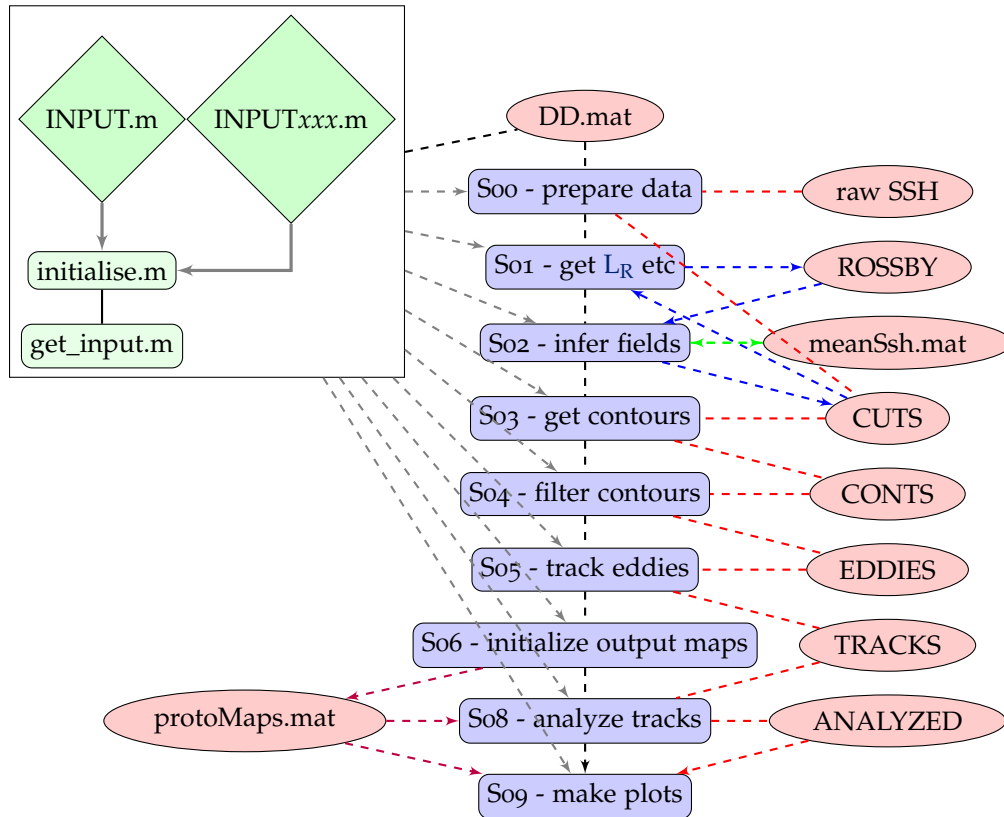


Figure 2.12: Basic code structure. The only files that are to be edited are the INPUT files. INPUT.m is independent of the origin of data, whilst the files INPUTaviso.m, INPUTpop.m etc set are samples of more source-specific parameter settings. Each of the SXX-steps initially calls initialise.m, which in turn scans all available data, reads in the INPUT data via get_input.m, corrects for missing data etc and creates DD.mat. The latter is the main meta-data file, which gets updated throughout all steps. All data is built step-by-step along the consecutive SXX-steps (red line). The SXX-steps are the only programs that have to be called (in order) by the user. Beware that missing data (in time) is interpolated automatically in each step. Note also that meanSsh.mat should be recalculated if the time span is changed!

3

Results

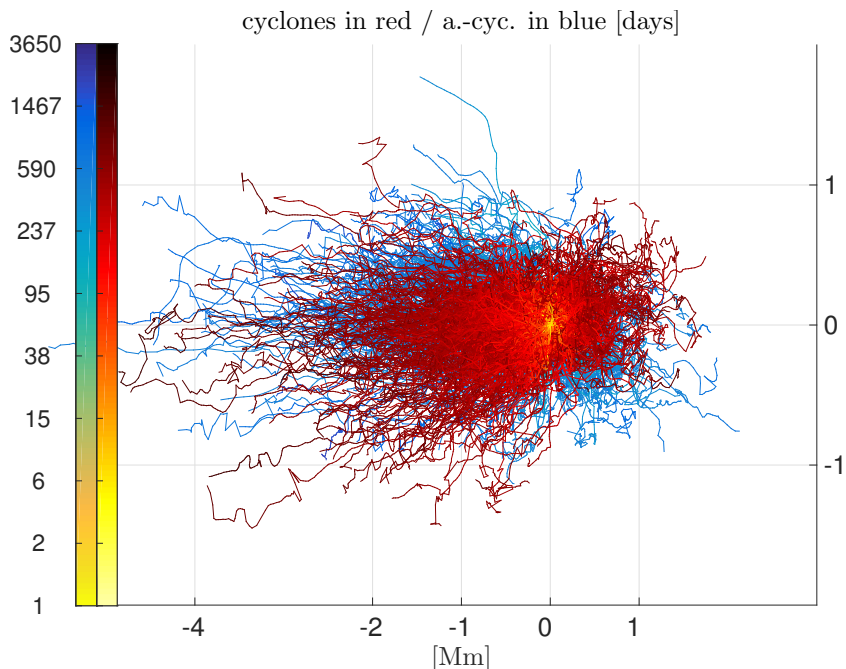


Figure 3.1: [Aviso -MI](#): Baseline-shifted *old* tracks. Tracks younger than 500days **TODO:**!
omitted.

THE short time frame and limited computational resources allowed for only a few complete global runs over the available data. It was therefore critical to carefully choose which method/parameters to use in order to maximize the deducible insight from the results. For best comparability of the results with each other it was decided to agree on one complete set of parameters as a basis (table 3.1), which

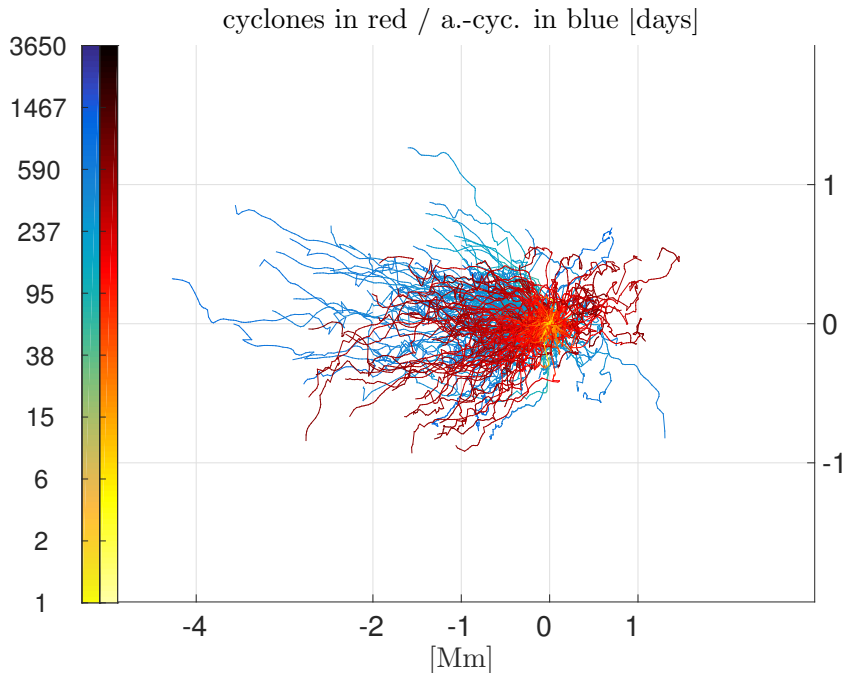


Figure 3.2: [Aviso -MII](#): Baseline-shifted *old* tracks. Tracks younger than 500days **TODO: !** omitted.

would then be altered at key parameters. The first run is an attempt to reproduce the results from [Chelton et al. \(2011\)](#). The SSH-data for this run is therefore that of the [Aviso](#) product. This method will be called **MII**.

THE second run (**MII**) is equivalent, except that this time the alternative **IQ**-based shape filtering method from [TODO ref](#) and the slightly different tracking-filter as described in [TODO: ref](#) are used. **MII** is then fed with 7-day time-step [POP](#) data as well.

To INVESTIGATE what role spatial resolution plays, the [POP](#) data was remapped to that of the [Aviso](#) data and fed to the **MII** method.

FINALLY , to investigate the effects of resolution in time, an **MII-1-day**-time-step run over [POP](#) data was executed. **TODO: POP-1day-MII-Southern-Ocean**

START AND END DATES were fix for all runs as the intersection of availability of both data sets.

time frame	1994/01/05 till 2006/12/27
scope	full globe (80S : 80N 180W : 180E)
Aviso geometry	641x1440 true Mercator
POP geometry	2400x3600
contour step	0.01
thresholds	[all SI]
max σ / L_R	4
min L_R	20e3
min IQ	0.55
min number of data comprising found contour	8
max(abs(Rossby phase speed))	0.2
min amplitude	0.01

Table 3.1: Fix parameters for all runs.
TODO: SI

TODO: Chelton's identity check takes Leff?

Box 2: Method MI

The concepts used in this method are mostly based on the description of the algorithm described by [Chelton et al. \(2011\)](#) and all parameters are set accordingly. Basically MI is a modification of MII (which was completed first), with the aim to try to recreate the results from [Chelton et al. \(2011\)](#). It differs from MII in the following:

- **detection**

As mentioned in TODO ref, the approach by [Chelton et al. \(2011\)](#) is to avoid overly elongated objects by demanding:

- high latitudes

The maximum distance between any vertices of the contour must not be larger than 400km for $|\phi| > 25^\circ$.

- low latitudes

The 400km-threshold increases linearly towards the equator to 1200km.

- **tracking**

The other minor difference to MII is in the way the tracking algorithm flags eddy-pairs between time-steps as sufficiently similar to be considered successful tracking-candidates (see TODO ref). In this method an eddy B from time-step $k + 1$ is considered as a potential manifestation of an eddy A from time-step k as long as both - the ratio of amplitudes (with regard to the mean of SSH within the found contour) and the ratio of areas (interpolated versions as discussed in TODO ref) fall within a lower and upper bound.

Box 3: Method MII

The purpose of this variant is basically to test the conceptually very different idea of the IQ-technique to test the shape of found contours for sufficiently eddy-typical. It also uses a slightly different tracking algorithm.

- **detection**

The IQ-method. See fig. 2.5 and filter 8.

- **tracking**

Conceptually similar to MI, it is again vertical and horizontal scales that are compared between time-steps. Preferring a single threshold-value over one upper and one lower bound, a parameter ξ was introduced that is the maximum of the two values resulting from the two ratios of amplitude respective σ , where either ratio is -if larger- its reciprocal in order to equally weight a decrease or an increase in respective parameter. In other words: $\xi = \max([\exp|\log R_\alpha|; \exp|\log R_\sigma|])$, where R are the ratios. **TODO: this has been explained twice now..**

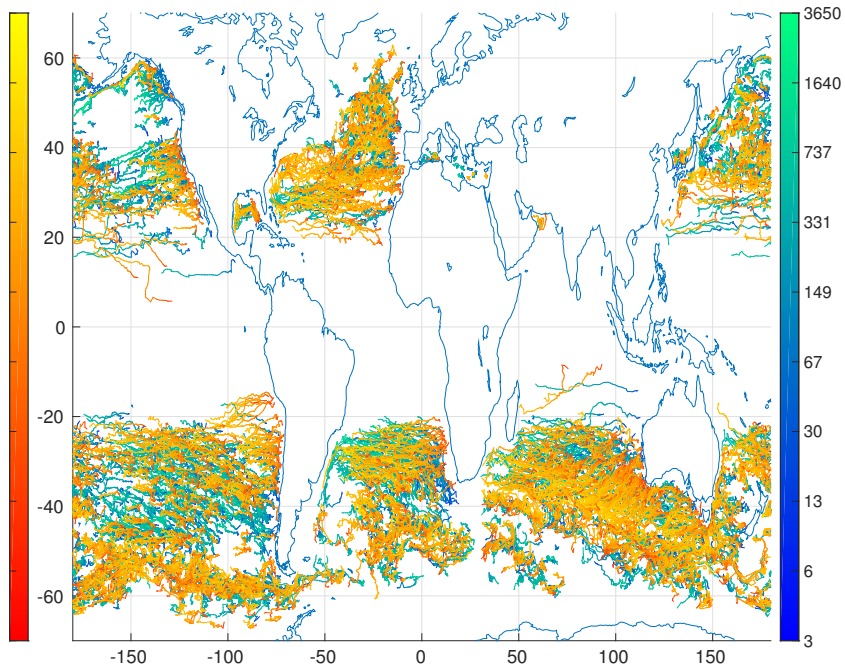


Figure 3.3: MI: anti-cyclones in red. Tracks younger than 1a omitted for clarity.

3.1 MI - 7 day time-step - Aviso

THE RESULTS from the MI-method are special in that they feature many long-lived eddies (see figs. 3.1, 3.3 and 3.5), some of which travelled more than 4000 km west. Tracks were recorded throughout the

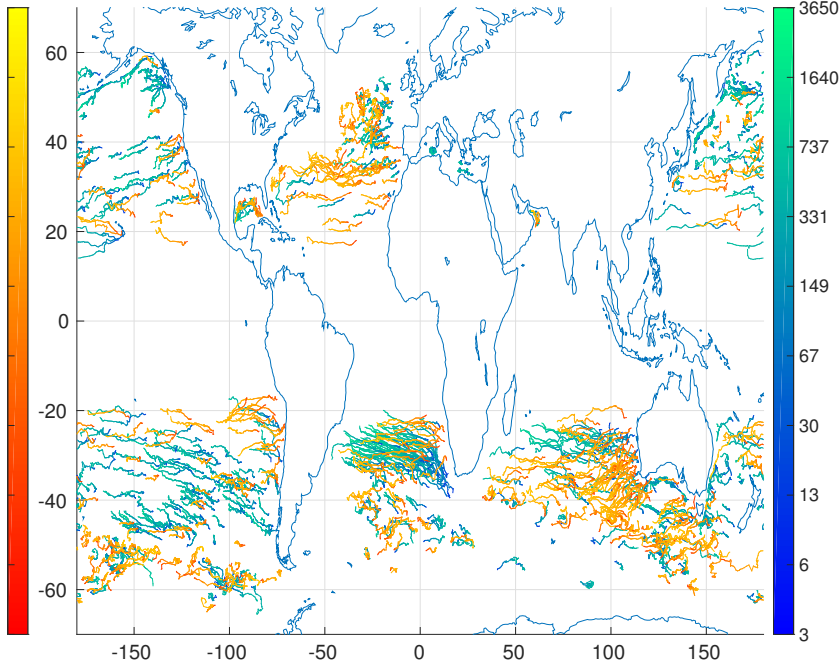


Figure 3.4: MII: anti-cyclones in red. Tracks younger than 1a omitted for clarity.

entire world ocean with the only exceptions being an approximately 20°-wide stripe along the equator. The highest count of unique eddies is along the Antarctic Circumpolar Current ¹ with counts of more than 60 individual eddy-visits per $1^\circ \times 1^\circ$ -cell. Further eddy-rich regions are the western North-Atlantic throughout the Gulf-Stream and North-Atlantic Current, *Mozambique eddies* (?) at 20° South along the Mozambique coast, along the Agulhas Current and south of the Cape of Good Hope at $\sim 40^\circ$, along the coasts of Brazil, Chile and all along the Eastern, Southern and Western coasts of Australia (see fig. 3.7).

¹ abbreviated ACC from here on.

EDDIES APPEAR AND DISAPPEAR throughout the world ocean. For long-lived solid eddies there is a tendency to emerge along western coasts (see ??).

THE SCALE σ of tracked eddies is similar to that in Chelton *et al.* (2011), yet generally smaller in high latitudes and slightly larger in low latitudes (see ??). It is larger than the first-mode baroclinic Rossby Radius by factor of at least 2 and its meridional profile appears to be separable into two different regimes; one apparently

linear profile in low latitudes and a steeper one equator-wards of $\sim |15^\circ|$. Regionally, locations of high mesoscale activity appear to correlate with smaller eddy-scales (see fig. 3.9).

THE EASTWARD ZONAL DRIFT SPEEDS are slightly slower than the first-mode baroclinic Rossby-Wave phase-speed and agree well with the results from Chelton *et al.* (2011). Propagation is generally westwards except for regions of sufficiently strong eastward advection as in the ACC and North Atlantic Current (see fig. 3.10 and ??).

places of birth and death. size indicates final age.

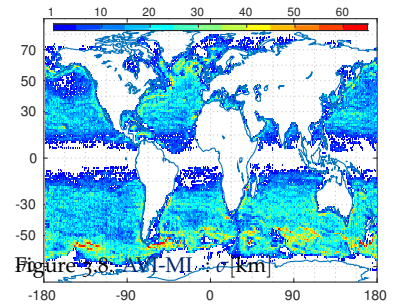
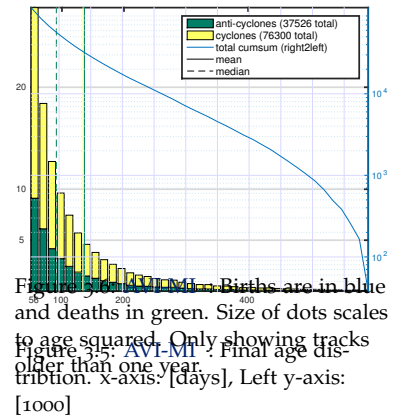
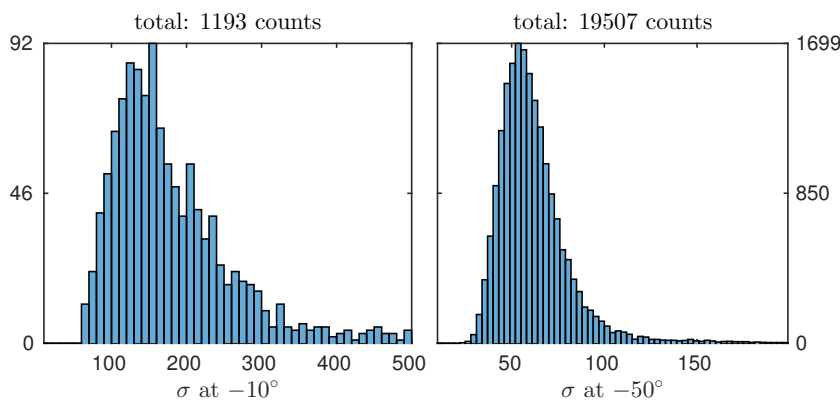
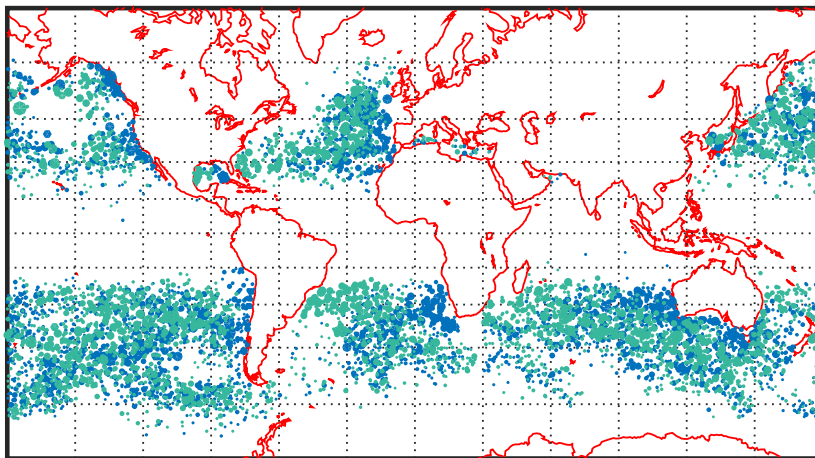


Figure 3.7: AVL-MI : Total count of individual eddies per 1 degree square.

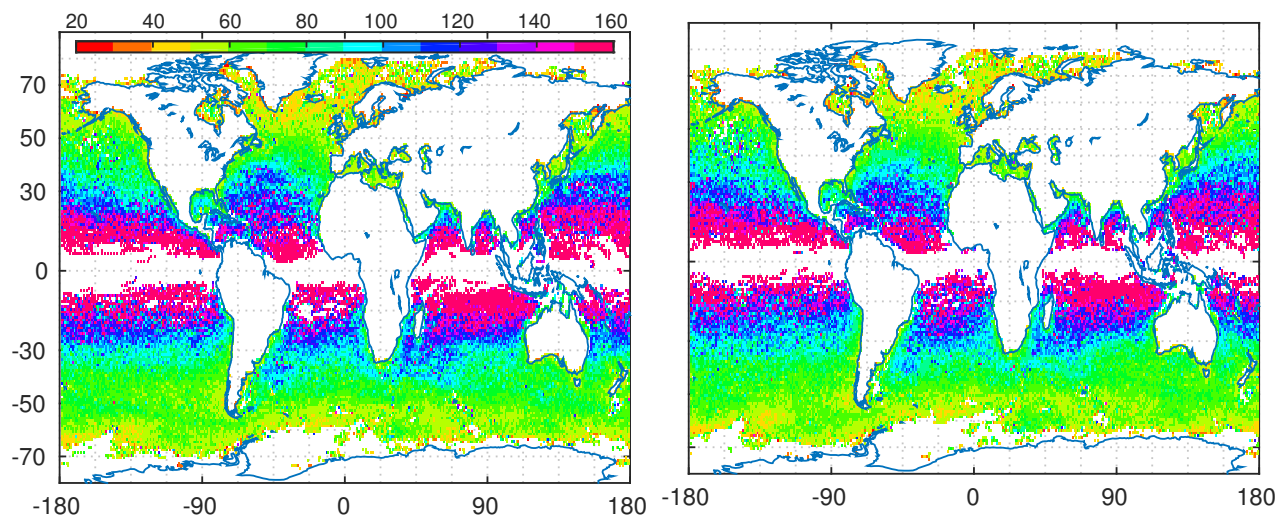
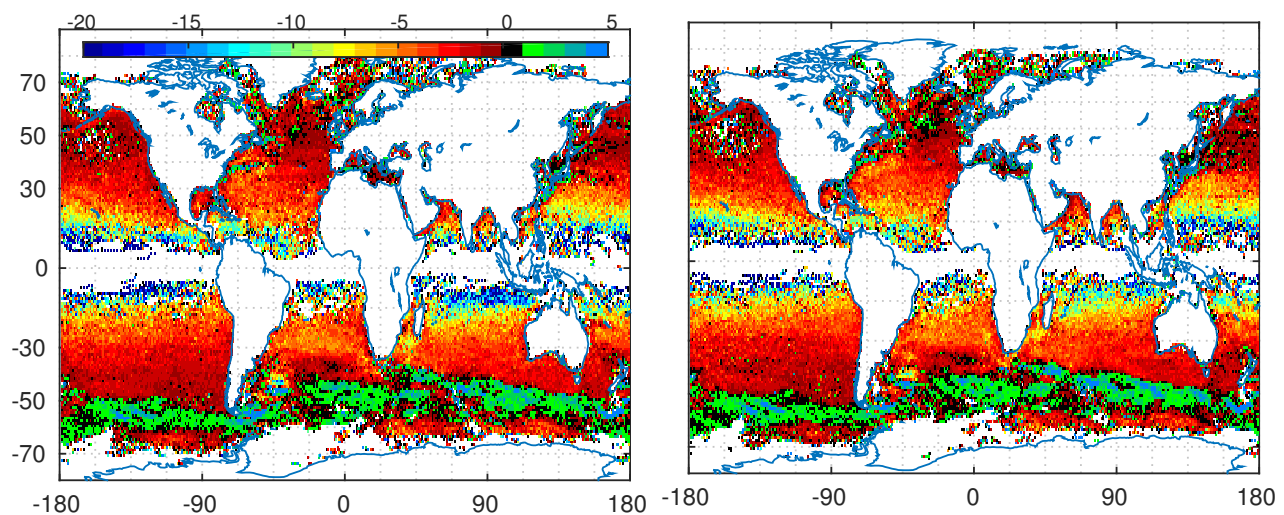
Figure 3.9: AVI-MI : σ [km]

Figure 3.10: AVI-MI : zonal translational speed [cm/s]

3.2 MII - 7 day time-step - Aviso

THE IQ-BASED METHOD results in approximately the same total amount of tracks as the MI-method used in section 3.1 (see figs. 3.5 and 3.11). The difference is that tracks here are generally much shorter, meaning that less eddies are detected at any given point in time.

THE SCALE σ is now smaller than that from Chelton *et al.* (2011) for all latitudes in zonal- mean as well as median.

WESTWARD DRIFT SPEEDS are almost identical to those in section 3.1.

places of birth and death. size indicates final age.

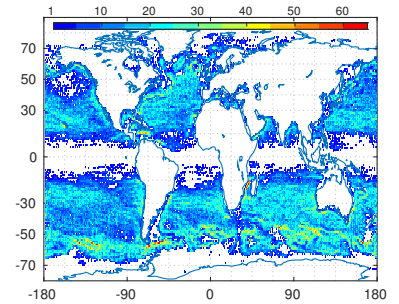
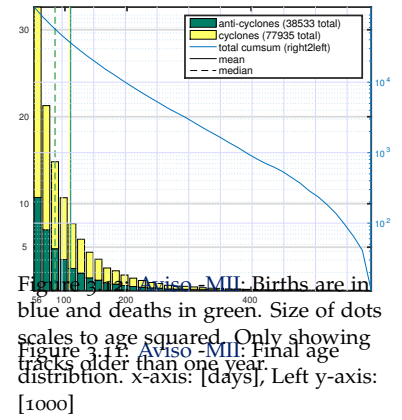
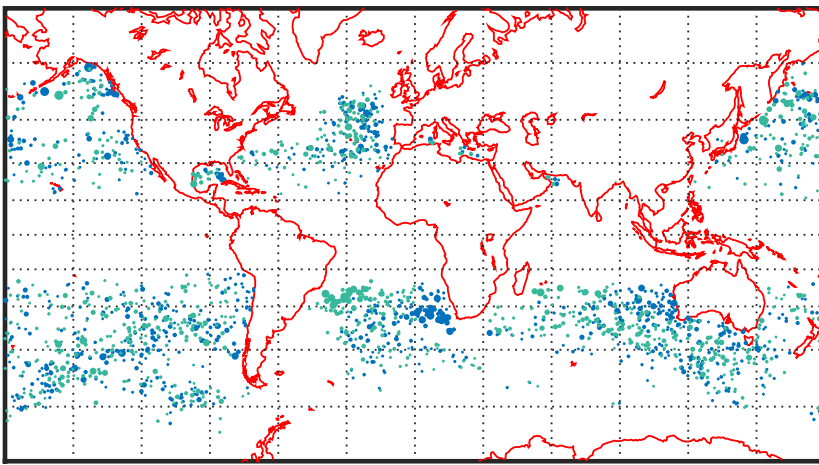


Figure 3.13: Aviso -MII: Total count of individual eddies per 1 degree square.

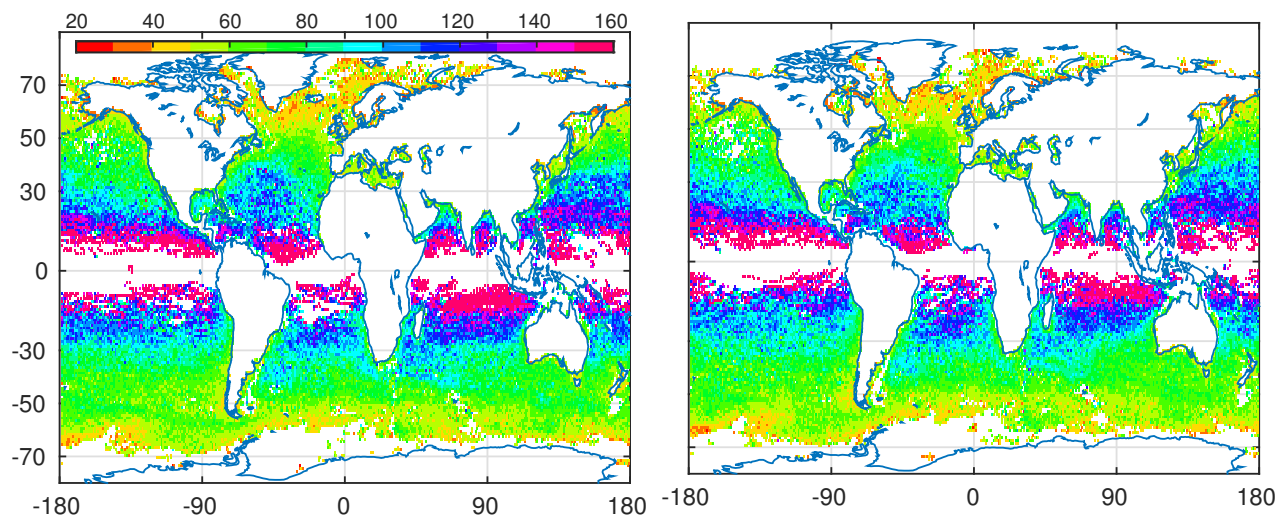
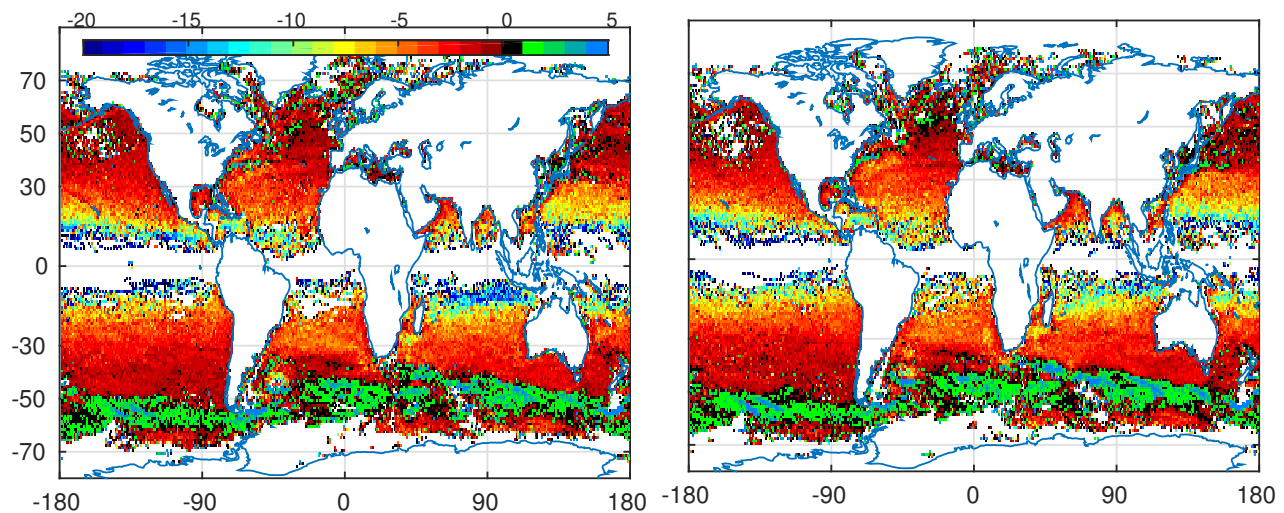
Figure 3.14: Aviso -MII: σ [km]

Figure 3.15: Aviso -MII: zonal translational speed [cm/s]

3.3 MII - 7 day time-step - POP

THE MODEL DATA delivers slightly more total tracks with a similar 2-fold dominance of cyclones over anti-cyclones (compare figs. 3.11 and 3.16). Similar to AVI-MII², very long tracks are fewer than via AVI-MI². The regional pattern looks somewhat similar to the satellite patterns in terms of which regions feature the strongest eddy activity, with the exception of an unrealistic abundance of eddies right along the Antarctic coast where no eddies were detected for the satellite data likely due to sea ice and/or the inherent lack of polar data due to the satellites' orbit-inclinations.

THE more important difference between model- and satellite regional distributions is that the model results indicate significantly less eddy activity away from regions of strong SSH gradients, in the open ocean away from coasts and strong currents. The algorithm also detects hardly any eddy tracks in tropical regions (see ??).

THE SCALE σ is generally smaller for the model-data-based analysis than for any satellite-based analyses, especially so in high latitudes.

WESTWARD DRIFT SPEEDS look regionally similar to those from satellite data (figs. 3.15 and 3.19). In the zonal mean their magnitude is below those from satellite (see fig. 3.22).

² AVI-MI features 3000 tracks that are older than 400 days, while both MII methods have only ~ 1000 of such.

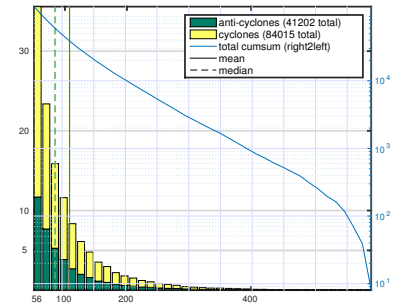


Figure 3.16: pop7-MII: Final age distribution. x-axis: [days], Left y-axis: [1000]

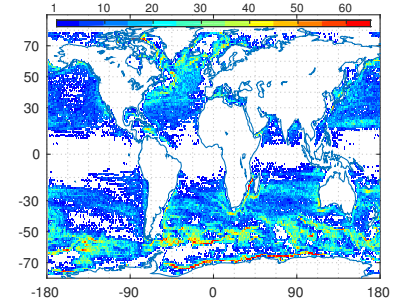


Figure 3.17: pop7-MII: Total count of individual eddies per 1 degree square.

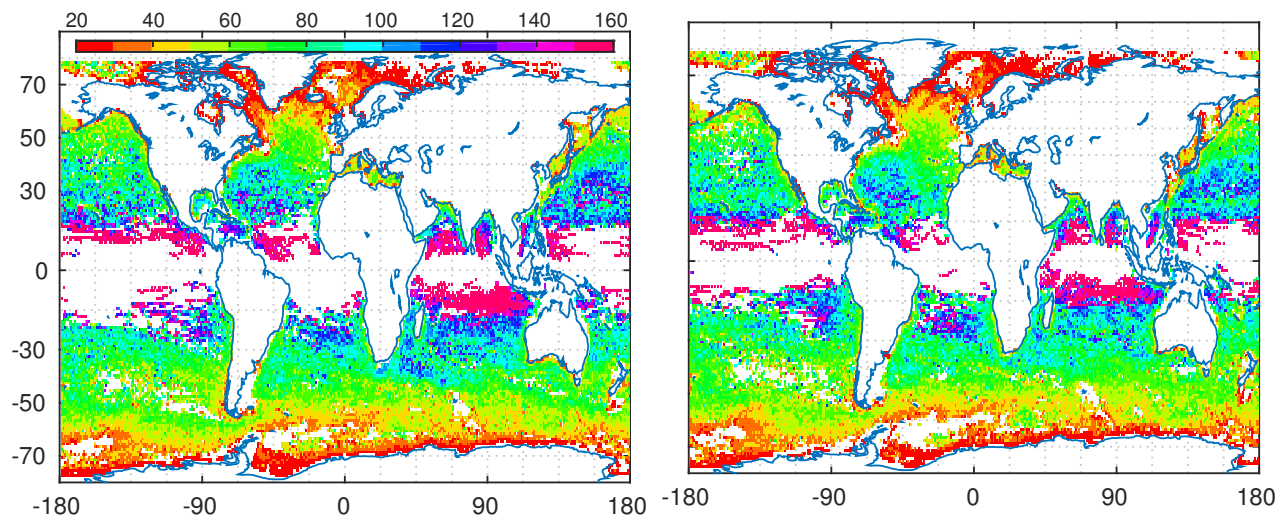
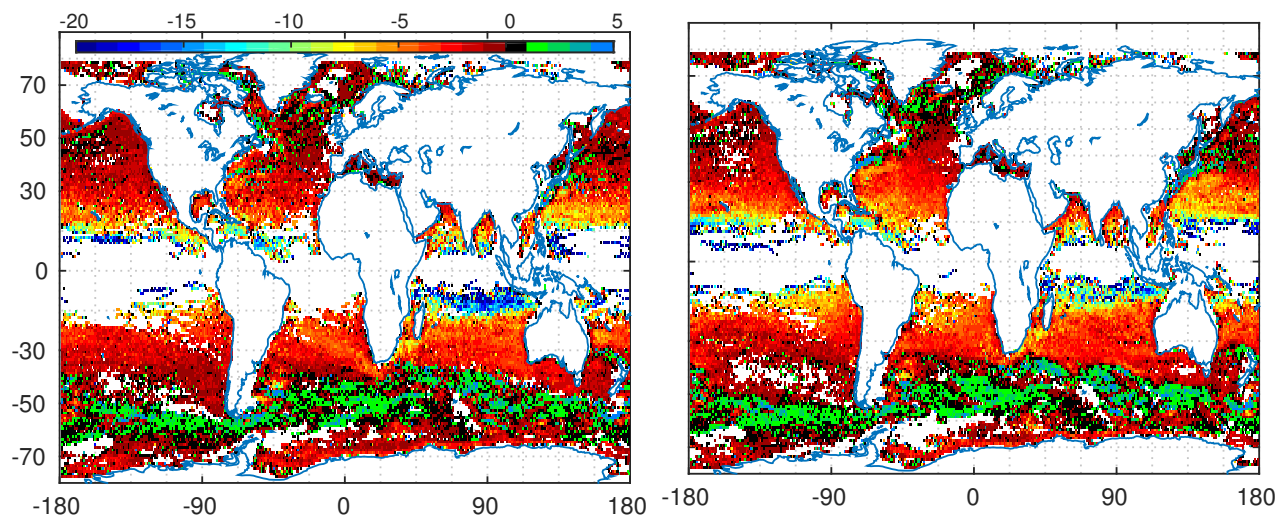
Figure 3.18: pop7-MII: σ [km]

Figure 3.19: pop7-MII: zonal translational speed [cm/s]

3.4 MII - 7 day time-step - POP remapped to Aviso geometry

THE MODEL DATA

THE SCALE σ

WESTWARD DRIFT SPEEDS

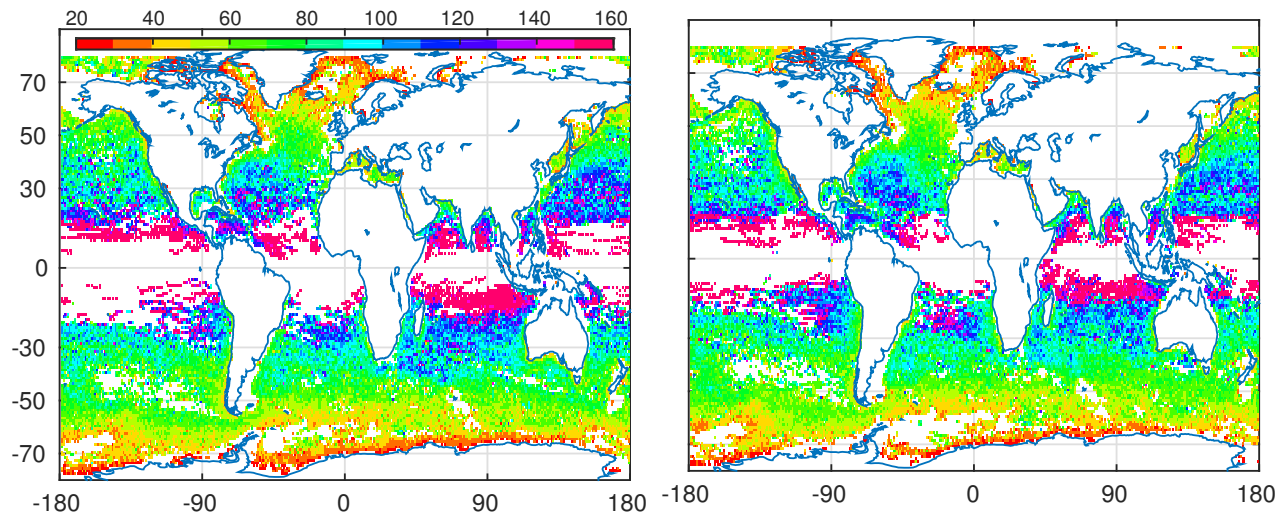


Figure 3.20: pop2aviso-MII: σ [km]

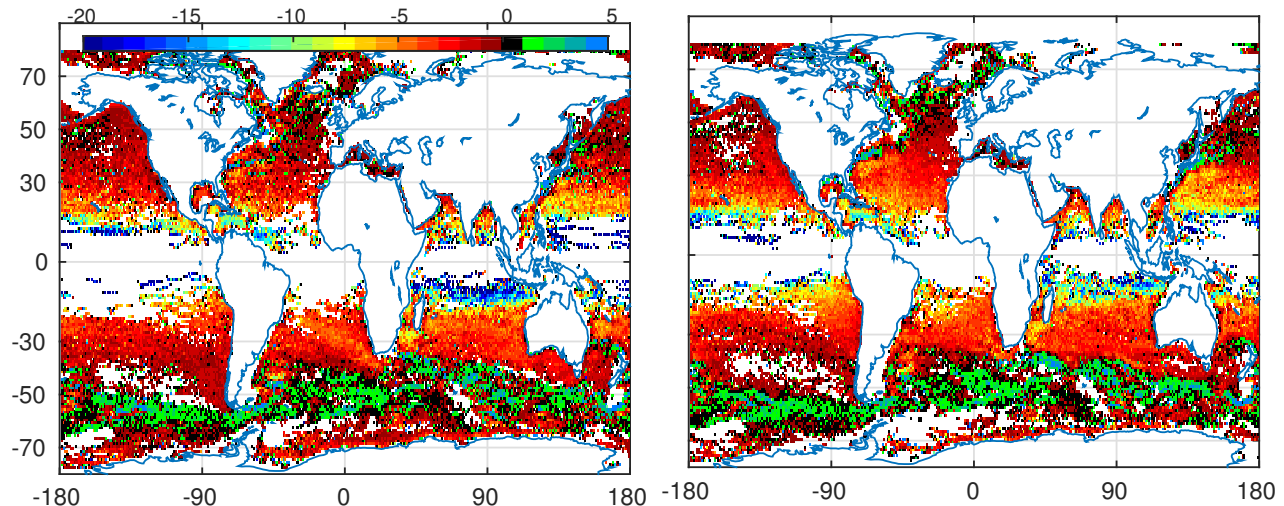


Figure 3.21: pop2aviso-MII: zonal translational speed [cm/s]

3.5 MII - 1 day time-step - POP

TODO: run is finished. Results will be looked at / interpreted next week

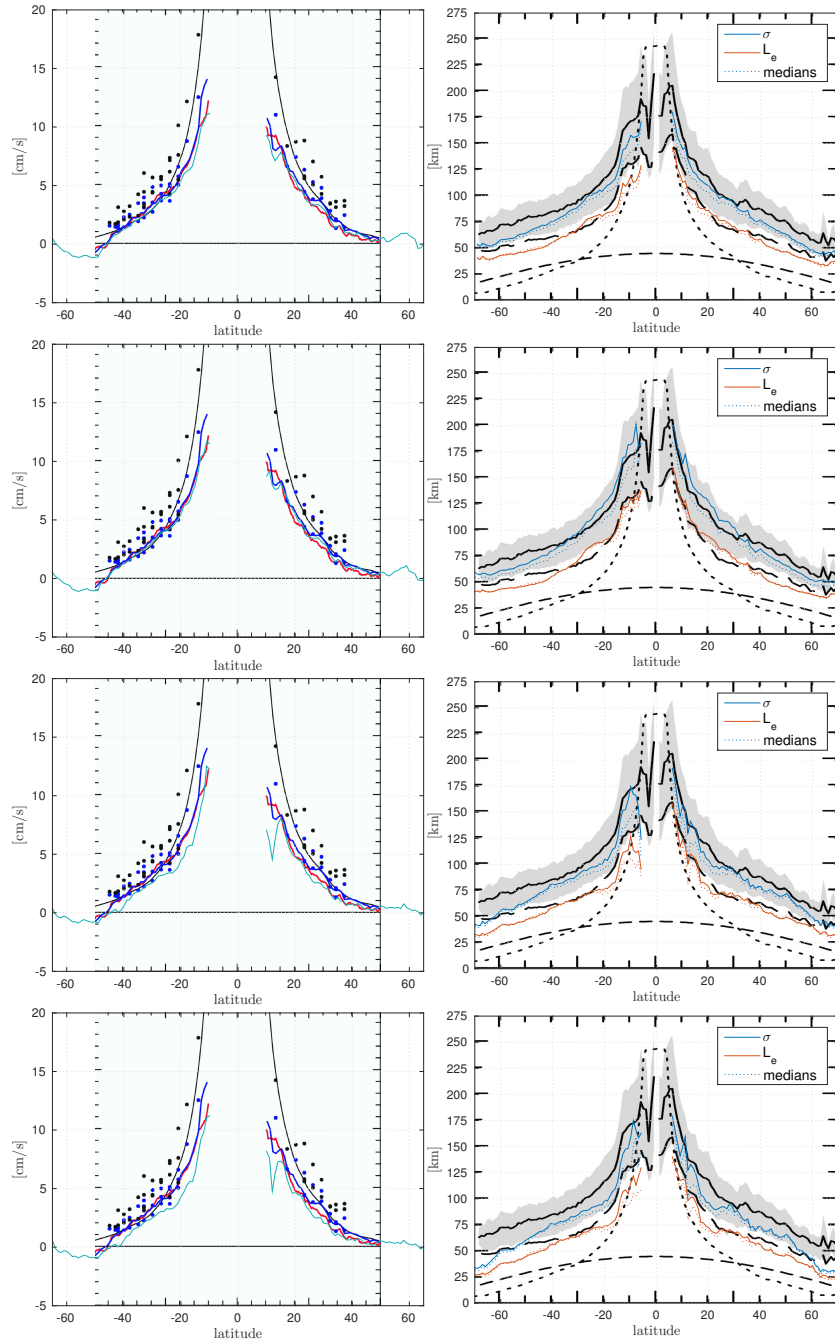


Figure 3.22: Left: Zonal-mean drift speed (cyan) fit to Fig 22 of (Chelton et al., 2011) (Background). Right: σ and L_e fit to Fig. 12 of their paper. Dotted lines are medians instead of means. 1st row: AVI-MII , 2nd row: AVI-MI , 3rd row: pop2avi-MII , 4th row: POP-7day-MII . Note that for the very high latitudes ($> |60^\circ|$) the contrast between model and satellite data is further intensified by the lack of satellite data (see figs. 3.14 and 3.18) in those regions (sea-ice / orbit inclinations). For a depiction without this effect see fig. 4.2.

4

Discussion

4.1 Lengths of Tracks

THE MOST APPARENT DIFFERENCE between the results of the **two detection-methods** is the abundance of long-lived eddies resulting from the **MI**-method. This discrepancy must logically be caused by the two different contour-shape-testing procedures (box 3 and filter 8), since it is here where the main difference between the two methods' algorithms lies.

THE **MI**-method is the more lenient one, as all it checks for, is whether the contour is of sufficiently compact form. The only shapes that are dismissed are long, thin elongated structures. This means that *e.g.* an eddy track can more easily¹ survive situations in which two eddies merge into one or those in which one is split into two or situations in which mean current gradients distort the vortex.

There could also be the situation in which an old, weak eddy fades, yet another one emerges in sufficient proximity. These two events would not even have to coincide at the exact same time, as long as some short-lived coherent structure, of which there is an abundance² at any given time-step throughout the world ocean, acted as a *bridge* to fill the gap.

THE **MII**-method is conceptually different in that it is based on the assumption that a distinct coherent vortex need *per definition* to be more or less circular. It will therefore be more likely to regard *e.g.* the situation in which one eddy merges with another as a situation of 3 eddies in total; **two** that have just died to create **one** new one. The

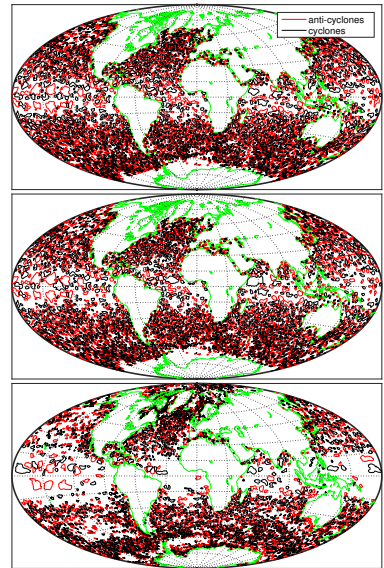


Figure 4.1: All contours that passed the filtering procedure for one exemplary time-step. Top: **AVI-MI**. Mid: **AVI-MII**. Bottom: **POP-7day-MII**.

¹ as long as the similarity-criterion is not violated.

² see ??

focus here is more on the propagation of distinct circular geostrophic vortices whereas the focus in the MI-method is more general on coherent local depressions respective elevations in SSH. Unfortunately the time-frame of this work did not allow to test to which degree tracers³ found within tracked eddies remained within the eddy over time. This could further clarify the assumption that the MI-method may be better at tracking water-mass advecting entities, with less jumps between bodies of water within one track.

4.2 Scales and the Effect of Downsampling

INTERESTINGLY, even in the AVI-MI results, the horizontal eddy scale σ differs from that presented by Chelton *et al.* (2011). For latitudes $\gtrsim |25^\circ|$ the zonal mean here is smaller than theirs while for low latitudes it is higher (see fig. 3.22). The reason for this discrepancy is suspected to stem from the special method by which σ is determined by our algorithm. As outlined in filter 12, here σ is half the mean of zonal and meridional distances between the first two local extrema of the first derivative of interpolated 4th-order fourier fits to the SSH data around the eddy's CoV.

THE motivation to use fits instead of the SSH directly was on the one hand to avoid noise complicating correct determinations of the 2nd differential zero-crossings and on the other hand to tackle the problem of coarse resolution, especially so for high latitudes where σ seems to become as small as only twice the distance between data points. At this resolution the Gaussian RMS width of an eddy would amount to only 5 data points. Since σ is generally smaller in the higher-resolution POP-data analyses, we hypothesize that the scales by Chelton *et al.* are biased high for high latitudes. Question remains to what degree this bias is inherent to the Aviso product *i.e.* as a smearing effect from the interpolation of multiple coarse satellite data. Or whether it is attributable entirely to the particular method by which the diameter/area of the zero-vorticity contour is estimated.

STRONG zonal skewness suggests the existence of many small, potentially erroneous values that smear the distribution of drift speeds towards an unrealistically low mean. This effect appears to be relevant in *e.g.* the Souther Ocean, where the east-ward advection of

³ in the model data.

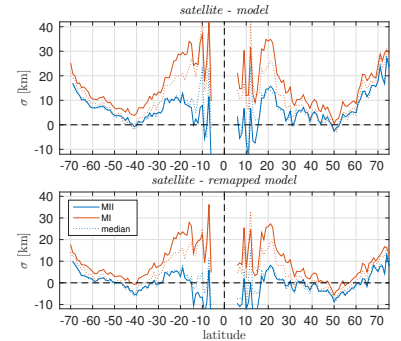


Figure 4.2: Differences in zonal mean σ between Aviso/POP and Aviso/downsampled POP. Means/Medians are built zonally over only those $1^\circ \times 1^\circ$ -bins that feature data in both sets *i.e.* the intersection of $lat + 1i\ lon$ of both sets.

eddies by the ACC results in a broad spectrum of drift speeds. The strong gradients in mean current also effect an abundance of eddy-merging and -splitting situations over relatively short periods of time. It is therefore difficult for the algorithm to keep track of sufficiently long-lived, coherent vortices. Especially so for large time-steps and a high age-threshold. Yet, if the minimum time-step is limited, as in the case of satellite data, a high age-threshold is necessary since short tracks with few data points in time are more likely to stem from erroneously matched contours that do not represent the actual track of a single vortex but instead represent other mesoscale noise that happened to feature sufficiently similar blobs popping in and out of existence at sufficient proximity to one another.

WITH REGARD to the lower latitudes two important aspects need to be considered:

1. The analyses yield generally low eddy activity in the tropics. Hence the results are less robust in this region *a priori*.
2. The standard deviation in σ is particularly broad in the tropics (see fig. 4.3). As a matter of fact it appears as though there might be two different types of eddies. One type analogous to all high-latitude eddies and a new one of much larger scale. Because these larger eddies have generally low IQ-values they are filtered from the MIIanalyses, resulting in smaller tropical σ . Their more chaotic shape might, due to the different methods to determine σ , also have to do with why mean tropical σ is larger here than in Chelton *et al.* (2011).

THE POP-7day-MII analysis yields somewhat similar σ for low latitudes⁴, yet significantly smaller values for high latitudes. The question here therefore is whether this discrepancy is a result of the lower resolution of the satellite data *i.e.* that eddies are too small to be resolved by the Aviso product in high latitudes or whether it is attributable to the model data as in a systematic bias due to incom-

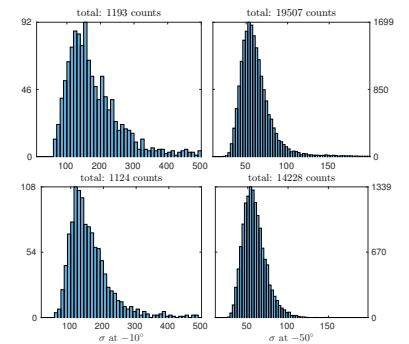


Figure 4.3: Eddy count at one point in time for one fully zonal 1°-bin. Top: AVI-MI . Bottom: AVI-MII . The tropical spectrum is broad yet with strong positive skewness *i.e.* oriented towards smaller scales. In high latitudes the standard deviation is smaller. The MImethod yields more large eddies.

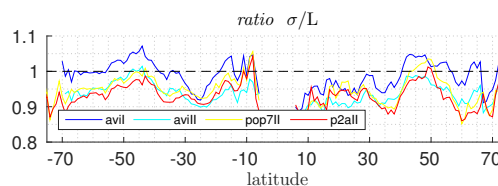


Figure 4.4: Ratios of σ to L (see filter 10)

⁴ Note that due to the lack of tropical eddies the estimates of σ are rather uncertain for the POP analyses.

plete/poorly parameterized model physics. This question was the primary motivation for the [pop2avi-MII](#)-analysis. The idea here was to down-size the POP data to the geometry of the [Aviso](#) grid in order to test whether this would raise σ to that from the satellite results. Figure 4.2 shows that the down-sampling did indeed decrease the discrepancy in σ to respective [Aviso](#) analysis, as long as those regions that are unique to either data set are excluded. Between $\pm 25^\circ$ and $\pm 65^\circ$ the difference is no larger than ± 5 km. This came as a surprise because since σ stems from Fourier fits of SSH, we expected the original frequencies to be, at least to some extent, conserved in the down-sampled data.

4.3 Profiles

THE [MIdetection](#) method a priori assumes that an eddy is more or less detected at its asymptotic *floor* i.e. in the case of an [AC](#) at the *foot of the mountain*. The idea of the [IQ](#)-based method on the other hand is to assume that the situation of a single well-defined eddy sitting on an otherwise smooth, flat sea surface, which would be necessary for the contour algorithm to find a closed contour describing the outermost perimeter of said single vortex, is unrealistic. Instead the approach is to look for distinct, sufficiently circular *caps* of SSH-hills/valleys that consistently *wade* through all other weaker geostrophic noise surrounding it.

TODO: why gaussian or quad? Read [Zhang et al. \(2013\)](#); [Centre et al. \(2001\)](#)

TODO: explain figs. 4.4 and 4.5

4.4 Drift Speeds

ZONAL MEAN DRIFT SPEEDS of all [Aviso](#) results agree well with those presented by [Chelton et al. \(2011\)](#) (see fig. 3.22), suggesting that the tracking procedures are relatively robust for both the [MIdetection](#) and [MII](#) methods.

THE [POP-7day-MII](#) results yield generally smaller magnitudes of u . The apparent drop in magnitude at $\sim 12^\circ\text{N}$ is most likely due to erroneous inter-time-step eddy-associations. In that region, the

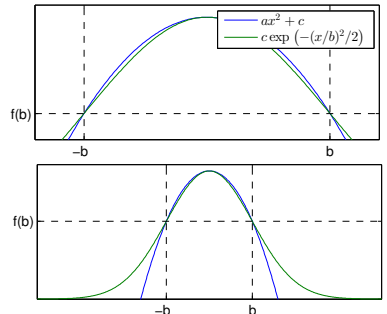


Figure 4.5: The upper part of a Gaussian profile can appear similar to a quadratic one. **TODO:** ref to here

combination of extreme sparsity of results, large time-step, large σ , low amplitude and high (theoretical) drift speed make robust determinations of u practically impossible. Yet the tendency for lower magnitudes in u , albeit less stark, is also true for higher latitudes. The zonal drift speeds are calculated via gradients of *polyfits* to the CoV-locations on the surface of a spherical earth. This method was tested thoroughly and its robustness is further validated by the fact that the weaker u remains approximately the same after down-sampling for the `pop2avi-MII` run.

FROM equation (1.5) we know that at first approximation (planetary lift)

$$u \sim \beta \left(\frac{NH}{f_0} \right)^2 \quad (4.1)$$

Since β, H and f should have been set realistically in POP, it appears that the, evidently unrealistic, drift speeds in the model results stem from an unrealistic or poorly resolved (only 42 vertical layers in POP) density stratification $\frac{\partial \rho}{\partial z}$.

4.5 POP-1day-MII-Southern-Ocean

TODO: run is finished. Results will be looked at / interpreted next week

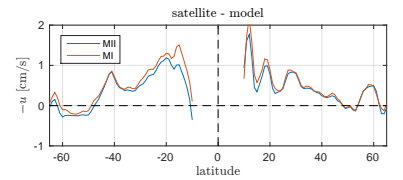


Figure 4.6: AVI-MI / AVI-MII minus POP-7day-MII of zonal drift speed means.

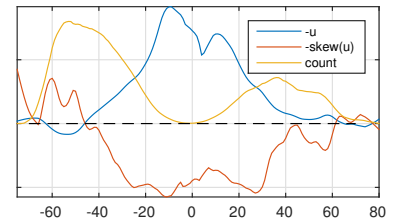


Figure 4.7: Skewness (red) of $-u$ for AVI-MI. The spectrum leans towards high westward values in low latitudes. In the ACC the distribution reverses indicating the existence of sporadic events of strong eastward advection by the mean flow. (Note: Everything normalized to fit all in one frame.)

5

Conclusion

5.1 POP-1day-MII-Southern-Ocean

TODO:

5.2 things to do bla

TODO: more data, depths, surface intensified, upper layer

TODO:

Further study in refining this structure is expected, and the refined structure can serve as a benchmark for numerical models where mesoscale eddies are explicitly resolved. In addition, the generation mechanism for this universal structure remains unknown; thus, exploring such mechanism may bring new excitement to eddy research.

[Zhang et al. \(2013\)](#)

TODO: 3d structure still mystery

TODO: H/f contours

TODO: tracers AC/C diff

A

Turbulence Aspects

THE horizontal scales of planetary geostrophic turbulence are usually so much larger than the vertical, that due to the gyroscopic rigidity of fluid motion in a rotating frame of reference, the turbulence is practically invariant in the vertical. Two-dimensional motion has the odd, counter-intuitive quality of cascading towards **larger** instead of **smaller** scales, as would be expected from 3-dimensional flow. This appendix is an attempt to explain this peculiar phenomenon heuristically.

$$\frac{Du}{Dt} + \Omega \times u = -\frac{1}{\rho} \nabla p + v \nabla^2 u + g \quad (\text{A.1a})$$

$$\frac{Dm}{Dt} = 0 \quad (\text{A.1b})$$

$$\frac{D\omega_a}{Dt} = (\omega_a \cdot \nabla) u + B + v \nabla^2 \omega \quad (\text{A.1c})$$

$$\frac{DE_k}{Dt} = -u_h \cdot \frac{1}{\rho} \nabla_h p + v \left(\frac{1}{2} \nabla^2 u^2 - \|\nabla u\|^2 \right) \quad (\text{A.1d})$$

$$\frac{DE_m}{Dt} = v \left(\frac{1}{2} \nabla^2 u^2 - \|\nabla u\|^2 \right) \quad (\text{A.1e})$$

$$\frac{D\varepsilon}{Dt} = \omega \cdot (\omega_a \cdot \nabla) u + \omega \cdot v \nabla^2 \omega \quad (\text{A.1f})$$

CONSIDER the equations of motion on a rotating spherical planet with all body forces combined in g , which shall always be perpendicular to the surface of a Newtonian fluid at rest. Applying the curl to equation (A.1a) also yields a vorticity equation¹. Scalar multiplication with u reveals a prognostic, kinetic-energy-per-unit-mass budget². Analogously, scalar multiplication of equation (A.1c) with ω_a yields an equation for the macroscopic enstrophy density per unit mass³. Finally, adding a term for potential energy to equation (A.1d) yields an equation for mechanical energy⁴.

¹ see [Derivation derivation 1](#)

² see [Derivation derivation 3](#)

³ see [Derivation derivation 4](#)

⁴ see [Derivation derivation 2](#)

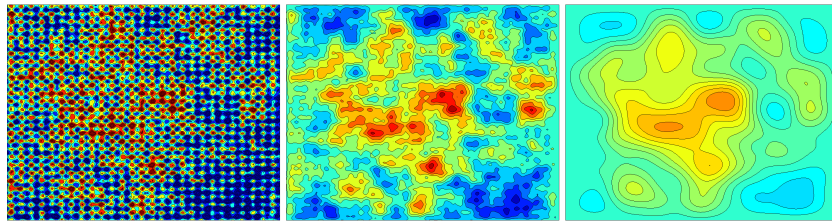


Figure A.1: 1) 2D turbulence with several sinusoidal and random signals as initial condition, 2) at a later time 3) at a much later time. Code from [Seibold \(2008\)](#).

Turbulence A.1: Non-rotating Tank

CONSIDER first a 3 dimensional non-rotating volume of fluid of constant density with horizontal and vertical dimensions of equal scale. Equations (A.1) then reduce to (ignoring E_k):

$$\frac{Du}{Dt} = -\frac{1}{\rho} \nabla p + \nu \nabla^2 u + g \quad (\text{A.2a})$$

$$\nabla \cdot u = 0 \quad (\text{A.2b})$$

$$\frac{D\omega}{Dt} = (\omega \cdot \nabla) u + \nu \nabla^2 \omega \quad (\text{A.2c})$$

$$\frac{DE_m}{Dt} = \nu \left(\frac{1}{2} \nabla^2 u^2 - \|\nabla u\|^2 \right) \quad (\text{A.2e})$$

$$\frac{D\varepsilon}{Dt} = \omega \cdot (\omega \cdot \nabla) u + \omega \cdot \nu \nabla^2 \omega \quad (\text{A.2f})$$

If we further assume the viscosity ν of the fluid to be infinitely small, equation (A.2e) and equation (A.2f) reduce to

$$\frac{DE_m}{Dt} = 0 \quad (\text{A.3e})$$

$$\frac{D\varepsilon}{Dt} = \omega \cdot (\omega \cdot \nabla) u \quad (\text{A.3f})$$

IN the absence of friction the mechanical Energy of the parcel of fluid is conserved. In contrast, neither enstrophy nor vorticity itself are conserved. Velocity gradients will tilt and stretch the parcel resulting in changes in relative vorticity so as to conserve the parcel's total angular momentum. There is no preference for dimension. The motion is simply turbulent akin to air blowing through a room.

Turbulence A.2: Rotating Tank

Next consider the tank from turbulence A.1 to be rotating at some high constant frequency $\Omega/2 \cdot \hat{z}$, so that all terms void of Ω are small versus those containing Ω while all derivatives of Ω vanish for its constancy. Again, imagine some magical mix of body forces, so that $\mathbf{g} \cdot \hat{z} = -g$.

$$\frac{D\mathbf{u}_h}{Dt} = -\boldsymbol{\Omega} \times \mathbf{u}_h + g \nabla \eta \quad (\text{A.4a})$$

$$\frac{D\boldsymbol{\omega}}{Dt} = \Omega \frac{\partial \mathbf{u}}{\partial z} \quad (\text{A.4c})$$

$$\frac{DE_m}{Dt} = \nu \left(\frac{1}{2} \nabla^2 \mathbf{u}^2 - \|\nabla \mathbf{u}\|^2 \right) \quad (\text{A.4e})$$

$$\frac{D\varepsilon}{Dt} = \boldsymbol{\omega} \cdot \Omega \frac{\partial \mathbf{u}}{\partial z} \quad (\text{A.4f})$$

Equation (A.4a) reveals that in this case all motion must be perpendicular to $\boldsymbol{\Omega}$ and to pressure gradients. Hence $w \approx 0$ and \mathbf{u}_h in hydrostatic- and geostrophic balance. Equation (A.4c) shows how a stretched or squeezed water column by e.g. a change in water depth results in a dramatic change in relative vorticity. Equation (A.4e) and equation (A.4f) show that again energy is conserved for the $\text{Re} \gg 1$ case (since our perspective is from the rotating frame of reference, the angular momentum from the rotating tank is a priori irrelevant to E_m), and that local enstrophy of a Lagrangian parcel is dramatically changed as soon as the vertical dimension is forced upon the motion.

Turbulence A.3: Small Aspect Ratio

CONSIDER again the tank, only this time completely flattened, so that its horizontal extent is, say, 3 orders of magnitude larger than its vertical scale. All vertical motion then becomes insignificant and at first approximation the equations reduce to:

$$\frac{\partial \mathbf{u}}{\partial t} + \mathbf{u} \cdot \nabla \mathbf{u} = g \nabla \eta + \nu \nabla^2 \mathbf{u} \quad (\text{A.5a})$$

$$\frac{\partial \omega}{\partial t} + \mathbf{u} \cdot \nabla \omega = \nu \nabla^2 \omega \quad (\text{A.5c})$$

$$\frac{DE_m}{Dt} = \nu \left(\frac{1}{2} \nabla^2 \mathbf{u}^2 - \omega^2 \right) \quad (\text{A.5e})$$

$$\frac{D\varepsilon}{Dt} = \nu \left(\frac{1}{2} \nabla^2 \omega^2 - \|\nabla \omega\|^2 \right) \quad (\text{A.5f})$$

THE main point here is that now, for infinitely small viscosity, besides mechanical energy, now also enstrophy is materially conserved. Lacking a third dimension to stretch, squeeze or tilt into, a column of fluid has no mechanism by which to adapt to a change in depth or to a change in ambient vorticity. To investigate this situation further, a scale analysis of the equations of E_m and ε yields:

$$\frac{U^2}{T} + \frac{U^3}{L} = \frac{\nu U^2}{L^2} \quad (\text{A.6e})$$

$$\frac{U^2}{TL^2} + \frac{U^3}{L^3} = \frac{\nu U^2}{L^4} \quad (\text{A.6f})$$

APPARENTLY $\frac{DE_m}{Dt} \sim L^2 \frac{D\varepsilon}{Dt}$. Thus, the smaller L , the more effective vorticity is advected and burned. Hence enstrophy dominates the turbulence cascade towards smaller scales. Before E_m gets any chance to cascade itself to ever smaller scales, ε is already effectively burning vorticity at large k and thereby reducing kinetic energy faster than the turbulence cascade can fill the gap. E_m being proportional to U^2 cannot compete with ε at small scales since ε not only scales with U^2 but also with the squared reciprocal of the scale *itself*.

As an analogy I imagine an ice hockey arena being opened instantaneously to 500 people on ice-skates. At first the picture will be highly turbulent with lots of friction among skaters. Sooner or later though, people of like-minded preference for direction and speed are likely to form groups so as to avoid bumping into one another. At some point usually all the people form into one or few large eddies, with those wanting to go faster than others skating at larger radii than the more timid towards the center, whilst those on inadequate orbits get subjected to corrective advection via friction *i.e.* entrainment.

Turbulence A.4: β -effect

CONSIDER at last the inviscid rotating flat-disk-type tank this time in the shape of a shell of a sphere with again $\mathbf{g} \parallel \hat{\mathbf{z}}$ everywhere perpendicular to the surface at rest. Further assume a strong \mathbf{g} so that the $\boldsymbol{\Omega} \cdot \mathbf{y}$ component in the Coriolis term is dwarfed by hydrostaticity. Then with $f = f\hat{\mathbf{z}} \equiv (\boldsymbol{\Omega} \cdot \hat{\mathbf{z}}) \hat{\mathbf{z}}$ now from a Eulerian perspective:

$$\frac{\partial \mathbf{u}}{\partial t} = -\mathbf{u} \cdot \nabla \mathbf{u} - \mathbf{f} \times \mathbf{u} + g \nabla \eta \quad (\text{A.7a})$$

$$\frac{\partial \boldsymbol{\omega}}{\partial t} = -\mathbf{u}_h \cdot \nabla_h \boldsymbol{\omega} - v \frac{\partial \mathbf{f}}{\partial y} \quad (\text{A.7c})$$

A new term with opposite sign from the $\boldsymbol{\omega}$ -advection-term in y -direction arises in the vorticity budget, which is evidently most significant where f changes strongest meridionally, *i.e.* In proximity to the sphere's *equator*. Hence, if scales permit, relative vorticity can now also be altered by a change in latitude via conservation of (total) angular momentum.

B

Eddy Categories

Starting from the considerations for equations (A.7) and introducing a variable density, the momentum equations and the z-component of the vorticity equation read:

$$\left(\frac{\partial \mathbf{u}}{\partial t}\right)^i + (\mathbf{u} \cdot \nabla \mathbf{u})^{ii} + (f_0 \times \mathbf{u})^{iii} + (\beta y \times \mathbf{u})^{iv} = (-g \nabla h)^v \quad (\text{B.1a})$$

$$\nabla \cdot \mathbf{u} = 0 \quad (\text{B.1b})$$

$$\left(\frac{D\omega}{Dt}\right)^A + \left(\frac{Df}{Dt}\right)^B = \left(f \frac{\partial w}{\partial z}\right)^C + \left(\omega \frac{\partial w}{\partial z}\right)^D \quad (\text{B.1c})$$

Several balances between terms to maintain vortices are thinkable here:

Vortex B.1: Frontal Lenses

large: R_β, B_u, U

small: Ro, W

balance between: ii, iii and v

The case with strong density gradients, large current speeds and a Rossby number approaching unity is typical for the meandering tails of turbulent boundary currents and zonal jets as in the Gulf Stream respective cyclogenesis in the atmospheric jet stream. Technically the intrathermoclinic lenses (Cushman-Roisin *et al.*, 1990) and strong-density-gradient deep eddies e.g. *meddies* fall into this group as well. With strong stratification, small vertical displacements cause strong pressure gradients. The dynamics can be limited to some thin layer, bottom topography is of little relevance and the surface signal might be small, or misleading.

Vortex B.2: Small Mid-Latitude Geostrophic Eddies

large: R_β
 $\mathcal{O}1:$ Bu
small: Ro
balance between: *iii* and v

The true geostrophic eddy with $L \sim L_R \sim NH/f$.

Vortex B.3: Large Geostrophic Gyres

small: Ro, R_β, Bu
balance between: *iii, iv, v* and friction

The large-scale wind-driven ocean gyres. These can only be interpreted as an *eddy* from the Reynolds-averaged large-scale perspective. The motion is strongly f/H -contour guided and the β -effect is immediately apparent in their strong western boundary intensification.

Vortex B.4: the Rossby-wave-eddy

large: L
 $\mathcal{O}1:$ Bu
small: $Ro R_\beta$
balance between: *iii, iv* and v

In low latitudes quasi-geostrophy and hence a small Rossby number demand large L and/or small U . The pressure gradients and hence surface elevation is small. Due to the large meridional extent, slow time-scale and strong $f(y)$ -gradient, particles moving north or south experience strong changes in planetary vorticity. So much so, that in this regime geostrophic eddies and Rossby waves are no longer clearly separable phenomena.

Vortex B.5: tornado

large: $U, g', L_R, \text{Ro}, \text{Bu}, R_\beta$

small: L

balance between: ii and v

significant vorticity term: A and friction (not considered here)

This case is not really applicable to the ocean except for maybe the tropics where f vanishes (but v would become relevant) or on small scales in areas of strong tidal currents in combination with bathymetry i.e. tidal bores etc. In this case a pressure force would have to be balanced by a centrifugal force alone (e.g. bathtub).

C

Derivations

Derivation 1: Vorticity

With the identity

$$\begin{aligned} \mathbf{u} \cdot \nabla \mathbf{u} &= (\nabla \times \mathbf{u}) \times \mathbf{u} + \nabla |\mathbf{u}|^2 / 2 \\ &= \boldsymbol{\omega} \times \mathbf{u} + \nabla \mathbf{u}^2 / 2 \end{aligned} \quad (\text{C.1})$$

equation (A.1a) becomes

$$\begin{aligned} \frac{\partial \mathbf{u}}{\partial t} + \nabla |\mathbf{u}|^2 / 2 + (2\boldsymbol{\Omega} + \boldsymbol{\omega}) \times \mathbf{u} &= -\frac{1}{\rho} \nabla p + \nu \nabla^2 \mathbf{u} + \mathbf{g} \\ \frac{\partial \mathbf{u}}{\partial t} + \nabla |\mathbf{u}|^2 / 2 + \boldsymbol{\omega}_a \times \mathbf{u} &= -\frac{1}{\rho} \nabla p + \nu \nabla^2 \mathbf{u} + \mathbf{g} \end{aligned} \quad (\text{C.2})$$

Applying the curl operation to equation (A.1a) and assuming equation (A.1b) for an incompressible fluid yields and equation for the vorticity

$$\begin{aligned} \frac{\partial \boldsymbol{\omega}}{\partial t} + \nabla \times \nabla |\mathbf{u}|^2 / 2 + \nabla \times (\boldsymbol{\omega}_a \times \mathbf{u}) &= -\frac{1}{\rho} \nabla \times \nabla p - \nabla \rho^{-1} \times \nabla p + \nu \nabla \times \nabla^2 \mathbf{u} + \nabla \times \mathbf{g} \\ &= -\frac{1}{\rho} \nabla \times \nabla p - \nabla \rho^{-1} \times \nabla p + \nu \nabla \times \nabla^2 \mathbf{u} + \nabla \times \mathbf{g} \end{aligned} \quad (\text{C.3})$$

Annilating all $\nabla \times \text{grad}$ and $\nabla \cdot \nabla \times$ and making use of the identity

$$\nabla \times (\mathbf{A} \times \mathbf{B}) = \mathbf{A} (\nabla \cdot \mathbf{B}) - \mathbf{B} (\nabla \cdot \mathbf{A}) + (\mathbf{B} \cdot \nabla) \mathbf{A} - (\mathbf{A} \cdot \nabla) \mathbf{B} \quad (\text{C.4})$$

equation (C.3) becomes

$$\begin{aligned} \frac{\partial \boldsymbol{\omega}}{\partial t} + \nabla \times (\boldsymbol{\omega}_a \times \mathbf{u}) &= -\frac{\nabla \rho \times \nabla p}{\rho^2} + \nu \nabla \times \nabla^2 \mathbf{u} \\ \frac{\partial \boldsymbol{\omega}}{\partial t} + (\mathbf{u} \cdot \nabla) \boldsymbol{\omega}_a - \mathbf{u} (\nabla \cdot \boldsymbol{\omega}_a) - (\boldsymbol{\omega}_a \cdot \nabla) \mathbf{u} &= \mathbf{B} - \nu \nabla \times (\nabla \times (\nabla \times \mathbf{u})) \\ \frac{D \boldsymbol{\omega}_a}{Dt} &= (\boldsymbol{\omega}_a \cdot \nabla) \mathbf{u} + \mathbf{B} - \nu \nabla \times (\nabla \times \boldsymbol{\omega}) \\ &= (\boldsymbol{\omega}_a \cdot \nabla) \mathbf{u} + \mathbf{B} + \nu \nabla^2 \boldsymbol{\omega} \end{aligned} \quad (\text{C.5})$$

Scaling considerations based on the small aspect ratio e.g. noting that $\mathbf{B} \sim \nabla p \times \nabla \rho$ is at first approximation limited to the x, y plane and that $U/H \gg W/L$ and assuming $\omega_z \gg \omega_h$, leads to:

$$\frac{\partial \boldsymbol{\omega}}{\partial t} + \mathbf{u} \cdot \nabla \boldsymbol{\omega} + \beta v \hat{\mathbf{z}} = (\omega_z + f) \frac{\partial \mathbf{u}}{\partial z} + \mathbf{B} \quad (\text{C.6})$$

horizontal:

$$\begin{aligned} \frac{1}{T} \frac{U}{H} + \left(\frac{U}{L} + \frac{W}{H} \right) \frac{U}{H} &\sim \frac{U}{H} \frac{U}{L} + f \frac{U}{H} + \mathbf{B} \\ \Rightarrow \frac{U}{HT} + \frac{U^2}{LH} + \frac{UW}{H^2} &\sim \frac{U^2}{LH} + f \frac{U}{H} + \mathbf{B} \end{aligned} \quad (\text{C.7})$$

vertical:

$$\begin{aligned} \frac{U}{LT} + \frac{U^2}{L^2} + \frac{WU}{HL} + \beta V &\sim \frac{UW}{LH} + f \frac{W}{H} \\ \Rightarrow \frac{U}{LT} + \frac{U^2}{L^2} + \beta V &\sim \frac{WU}{HL} + f \frac{W}{H} \end{aligned} \quad (\text{C.8})$$

Hence at first order:

$$\frac{D \boldsymbol{\omega}_h}{Dt} = (f + \omega_z) \frac{\partial \mathbf{u}_h}{\partial z} + \mathbf{B} \quad (\text{C.9})$$

$$\frac{D \omega_z}{Dt} + \beta v = (f + \omega_z) \frac{\partial \omega}{\partial z} \quad (\text{C.10})$$

If we further assume quasi-geostrophic motion so that any change in ω_h is due to small ageostrophic parallelization of ∇p and $\nabla \rho$ via \mathbf{B} , the tilting terms vanish, since then ω_h is normal to the plane spun by $\nabla \mathbf{u}_h$ and $\nabla \omega$.

Derivation 2: Mechanical Energy

Add term for potential energy to equation (A.1d) (assuming $\nabla\rho = 0$)

$$\begin{aligned}
 \frac{DE_m}{Dt} &= -g\mathbf{u} \cdot \nabla\eta(x, y) + \nu \left(\frac{1}{2} \nabla^2 \mathbf{u}^2 - \|\nabla\mathbf{u}\|^2 \right) + \mathbf{u} \cdot \mathbf{g} \\
 \frac{DE_m}{Dt} &= -g\mathbf{u} \cdot \nabla\eta(x, y) + \nu \left(\frac{1}{2} \nabla^2 \mathbf{u}^2 - \|\nabla\mathbf{u}\|^2 \right) - wg \\
 &= -g \left(\frac{\partial\eta}{\partial t} + \mathbf{u} \cdot \nabla\eta \right) + \nu \left(\frac{1}{2} \nabla^2 \mathbf{u}^2 - \|\nabla\mathbf{u}\|^2 \right) \\
 &= -g \frac{D\eta}{Dt} + \nu \left(\frac{1}{2} \nabla^2 \mathbf{u}^2 - \|\nabla\mathbf{u}\|^2 \right) \\
 &= \nu \left(\frac{1}{2} \nabla^2 \mathbf{u}^2 - \|\nabla\mathbf{u}\|^2 \right)
 \end{aligned} \tag{C.11}$$

Derivation 3: Kinetic Energy

Multiply equation (A.1a) by \mathbf{u} :

$$\begin{aligned}
 \mathbf{u} \cdot \left(\frac{\partial\mathbf{u}}{\partial t} + \mathbf{u} \cdot \nabla\mathbf{u} + 2\Omega \times \mathbf{u} \right) &= -\mathbf{u} \cdot \frac{1}{\rho} \nabla p + \mathbf{u} \cdot \nu \nabla^2 \mathbf{u} + \mathbf{u} \cdot \mathbf{g} \\
 \frac{1}{2} \frac{\partial\mathbf{u}^2}{\partial t} + \frac{1}{2} \mathbf{u} \cdot \nabla\mathbf{u}^2 + \mathbf{u} \cdot 2\Omega \times \mathbf{u} &= -\mathbf{u} \cdot \frac{1}{\rho} \nabla p + \mathbf{u} \cdot \nu \nabla^2 \mathbf{u} - wg \\
 \frac{1}{2} \frac{\partial\mathbf{u}^2}{\partial t} + \frac{1}{2} \mathbf{u} \cdot \nabla\mathbf{u}^2 &= -\mathbf{u}_h \cdot \frac{1}{\rho} \nabla_h p + wg + \mathbf{u} \cdot \nu \nabla^2 \mathbf{u} - wg \\
 \frac{1}{2} \frac{\partial\mathbf{u}^2}{\partial t} + \frac{1}{2} \mathbf{u} \cdot \nabla\mathbf{u}^2 &= -\mathbf{u}_h \cdot \frac{1}{\rho} \nabla_h p + \mathbf{u} \cdot \nu \nabla^2 \mathbf{u} \\
 \frac{\partial E_k}{\partial t} + \mathbf{u} \cdot \nabla E_k &= -g\mathbf{u}_h \cdot \nabla\eta(x, y) + \nu \left(\frac{1}{2} \nabla^2 \mathbf{u}^2 - \|\nabla\mathbf{u}\|^2 \right)
 \end{aligned} \tag{C.12}$$

Derivation 4: Enstrophy

In 2 dimensions the definition of enstrophy can also be rewritten as:

$$\begin{aligned}
 \mathcal{E} &= \int_A \epsilon \, dA = \int_A \|\nabla \mathbf{u}\|^2 \, dA \\
 &= \int_A \left(\frac{\partial v}{\partial x} \right)^2 + \left(\frac{\partial u}{\partial y} \right)^2 + \left(\frac{\partial v}{\partial y} \right)^2 + \left(\frac{\partial u}{\partial x} \right)^2 \, dA \\
 &= \int_A \left(\frac{\partial v}{\partial x} \right)^2 + \left(\frac{\partial u}{\partial y} \right)^2 + \left(\frac{\partial v}{\partial y} \right)^2 + \left(\frac{\partial u}{\partial x} \right)^2 - (\nabla \cdot \mathbf{u})^2 \, dA \\
 &= \int_A \left(\frac{\partial v}{\partial x} \right)^2 + \left(\frac{\partial u}{\partial y} \right)^2 - 2 \frac{\partial u}{\partial x} \frac{\partial v}{\partial y} \, dA \\
 &= \int_A \omega^2 + 2 \frac{\partial u}{\partial y} \frac{\partial v}{\partial x} - 2 \frac{\partial u}{\partial x} \frac{\partial v}{\partial y} \, dA \\
 &= \int_A \omega^2 + 2 \frac{\partial u}{\partial y} \frac{\partial v}{\partial x} + 2 \left(\frac{\partial v}{\partial y} \right)^2 \, dA
 \end{aligned} \tag{C.13}$$

with $\nabla \cdot \mathbf{u} = 0$ and appropriate boundary conditions, the last two terms cancel in the integral leaving

$$\mathcal{E} = \int_A \omega^2 \, dA \tag{C.14}$$

Derivation 5: Vorticity Scales

Assuming approximate geostrophy and $Bu = \mathcal{O}(10^1)$:

$$\rho f U \sim \nabla p \tag{C.15}$$

in a layered model:

$$\begin{aligned}
 fU &\sim g' \nabla \eta \\
 U &\sim \frac{hN^2}{f} \nabla \eta \\
 U &\sim \frac{h^2 N^2}{fL}
 \end{aligned} \tag{C.16}$$

and hence

$$\begin{aligned}
 \omega &\sim U/L \sim \frac{h^2 N^2}{fL^2} \\
 &= f \frac{L_R}{L}
 \end{aligned} \tag{C.17}$$

TODO: take out

Derivation 6: vortex limitations

$$\mathbf{u} \cdot \nabla \mathbf{u} + f \mathbf{u} = -g \nabla \eta \quad (\text{C.18})$$

$$\begin{aligned} \frac{U^2}{L} + fU + \frac{gh}{L} &= 0 \\ U^2 + fLU + gh &= 0 \end{aligned} \quad (\text{C.19})$$

possible balances: cyclone

$$\text{sign}(F_c) = \text{sign}(F_p):$$

$$U_{1,2} = -fL/2 \pm \sqrt{f^2 L^2 / 4 + gh} \quad (\text{C.20})$$

anti-cyclone

$$\text{sign}(F_c) = -\text{sign}(F_p):$$

$$U_{1,2} = -fL/2 \pm \sqrt{f^2 L^2 / 4 - gh} \quad (\text{C.21})$$

$$\begin{aligned} 4gh &\leq f^2 L^2 \\ 2c &\leq fL \\ 2L_R &\leq L \end{aligned} \quad (\text{C.22})$$

TODO: take out

Derivation 7: Okubo-Weiss-Parameter

$$\begin{aligned} O_w = \text{Tr } \mathbb{T}^2 &= \left(\frac{\partial u_i}{\partial x_k} \frac{\partial u_k}{\partial x_j} \hat{e}_i \hat{e}_j \right)_{i,i} \\ &= \frac{\partial u_i}{\partial x_j} \frac{\partial u_j}{\partial x_i} \\ &= \left(\frac{\partial u_i}{\partial x_i} \right)^2 + (1 - \delta_{i,j}) \frac{\partial u_j}{\partial x_i} \frac{\partial u_i}{\partial x_j} \\ &= \left(\frac{\partial u_i}{\partial x_i} \right)^2 + \frac{1}{2} \left(\frac{\partial u_i}{\partial x_j} + \frac{\partial u_j}{\partial x_i} \right)^2 - \frac{1}{2} \left(\frac{\partial u_i}{\partial x_j} - \frac{\partial u_j}{\partial x_i} \right)^2 \\ &= \frac{1}{2} \left(\frac{\partial u_i}{\partial x_i} + \frac{\partial u_j}{\partial x_j} \right)^2 + \frac{1}{2} \left(\frac{\partial u_i}{\partial x_i} - \frac{\partial u_j}{\partial x_j} \right)^2 + \frac{1}{2} \left(\frac{\partial u_i}{\partial x_j} + \frac{\partial u_j}{\partial x_i} \right)^2 - \frac{1}{2} \left(\frac{\partial u_i}{\partial x_j} - \frac{\partial u_j}{\partial x_i} \right)^2 \\ &= \text{divergence}^2 + \text{stretch}^2 + \text{shear}^2 - \text{vorticity}^2 \end{aligned} \quad (\text{C.23})$$

See also section 1.1.1.

Derivation 8: Cushman's Zonal Drift Speeds

With

X : x-position of CoV

H : mean layer thickness

V_e : Volume $\int_A \eta \, dA$

$$\begin{aligned}
 X_t &= -\frac{\beta g' \int H\eta + \eta^2/2 \, dA}{\int \eta \, dA} \\
 &= -\frac{\beta g'}{f_0^2} \left(H + \frac{\int \eta^2/2 \, dA}{V_e} \right) \\
 &= -\frac{\beta c^2}{f_0^2} \left(1 + \frac{1}{H} \frac{\int \eta^2/2 \, dA}{V_e} \right) \\
 &= -\beta L_R^2 \left(1 + \frac{1}{H} \frac{\int \eta^2 \, dA}{2V_e} \right) \\
 &= \frac{\omega_{long}}{k} \left(1 + \frac{1}{H} \frac{\int \eta^2 \, dA}{2V_e} \right)
 \end{aligned} \tag{C.24}$$

(see section 1.2.2)

TODO: i took out Turbulent Kinetic Energy, Mean Fields of u and b

Declaration of Authorship

I, Nikolaus KOOPMANN, declare that this thesis titled, 'A Global Analysis of Mesoscale Eddy Dynamics via a Surface-Signature-Based Tracking Algorithm' and the work presented in it are my own. I confirm that:

- This work was done wholly or mainly while in candidature for a research degree at this University.
- Where any part of this thesis has previously been submitted for a degree or any other qualification at this University or any other institution, this has been clearly stated.
- Where I have consulted the published work of others, this is always clearly attributed.
- Where I have quoted from the work of others, the source is always given. With the exception of such quotations, this thesis is entirely my own work.
- I have acknowledged all main sources of help.
- Where the thesis is based on work done by myself jointly with others, I have made clear exactly what was done by others and what I have contributed myself.

Signed: _____

Date: _____

Bibliography

- Batchelor, George K. 1969. Computation of the Energy Spectrum in Homogeneous Two-Dimensional Turbulence. *Phys. Fluids*, **12**(12), II—233.
- Bjerknes, J, & Holmboe, J. 1944. O the Theory of Cyclones. *J. Atmos. Sci.*
- Brachet, ME. 1988. The dynamics of freely decaying two-dimensional turbulence. *J. Fluid*
- Bryan, K, Dukowicz, JK, & Smith, RD. 1999. On the mixing coefficient in the parameterization of bolus velocity. *J. Phys.* ..., 2442–2456.
- Centre, J M Burgers, Beckers, M., Verzicco, R., Clercx, H. J. H., & Van Heijst, G. J. F. 2001. Dynamics of pancake-like vortices in a stratified fluid: experiments, model and numerical simulations. *J. Fluid Mech.*, **433**(June), 1–27.
- Charney, JG. 1971. Geostrophic turbulence. *J. Atmos. Sci.*
- Chelton, Dudley B., Schlax, Michael G., Samelson, Roger M., & de Szoeke, Roland a. 2007. Global observations of large oceanic eddies. *Geophys. Res. Lett.*, **34**(15), L15606.
- Chelton, Dudley B., Schlax, Michael G., & Samelson, Roger M. 2011. Global observations of nonlinear mesoscale eddies. *Prog. Oceanogr.*, **91**(2), 167–216.
- Cipollini, Paolo, Cromwell, David, Jones, Matthew S, Quartly, Graham D, & Challenor, Peter G. 1997. Concurrent altimeter and infrared observations of Rossby wave propagation near 34 N in the North-east Atlantic. *Geophys. Res. Lett.*, **24**(8), 889–892.
- Cushman-Roisin, Benoit. 2010. *Introduction to Geophysical Fluid Dynamics*.
- Cushman-Roisin, Benoit, Tang, Benyang, & Chassignet, Eric P. 1990. Westward motion of mesoscale eddies. *J. Phys.* ..., **20**(5), 758–768.

- Eden, Carsten. 2006. Thickness diffusivity in the Southern Ocean. *Geophys. Res. Lett.*, **33**(11), L11606.
- Eden, Carsten. 2007a. Eddy length scales in the North Atlantic Ocean. *J. Geophys. Res.*, **112**(C6), C06004.
- Eden, Carsten. 2007b. Interpreting eddy fluxes. *J. Phys.* . . . , 1–34.
- Eden, Carsten. 2011. A closure for meso-scale eddy fluxes based on linear instability theory. *Ocean Model.*, **39**(3-4), 362–369.
- Eden, Carsten. 2012. Implementing diffusivities from linear stability analysis in a three-dimensional general circulation ocean model. *Ocean Model.*, **57**, 15–28.
- Eden, Carsten, & Greatbatch, Richard J. 2008. Towards a mesoscale eddy closure. *Ocean Model.*, **20**(3), 223–239.
- Eden, Carsten, Greatbatch, Richard J., & Willebrand, Jürgen. 2007. A Diagnosis of Thickness Fluxes in an Eddy-Resolving Model. *J. Phys. Oceanogr.*, **37**(3), 727–742.
- Ferrari, Raffaele, & Nikurashin, Maxim. 2010. Suppression of Eddy Diffusivity across Jets in the Southern Ocean. *J. Phys. Oceanogr.*, **40**(7), 1501–1519.
- Flierl, Glenn R. 1984. Rossby wave radiation from a strongly nonlinear warm eddy. *J. Phys. Oceanogr.*, **14**(1), 47–58.
- Forget, Gaël. 2010. Mapping Ocean Observations in a Dynamical Framework: A 2004–06 Ocean Atlas. *J. Phys. Oceanogr.*, **40**(6), 1201–1221.
- Fox-Kemper, Baylor, Ferrari, Raffaele, & Hallberg, Robert. 2008. Parameterization of Mixed Layer Eddies. Part I: Theory and Diagnosis. *J. Phys. Oceanogr.*, **38**(6), 1145–1165.
- Gaspar, Philippe, Grégoris, Y, & Lefevre, JM. 1990. A simple eddy kinetic energy model for simulations of the oceanic vertical mixing. . . *Res. Ocean.* (1978– . . . , **95**, 179–193.
- Gent, Peter R, & Mcwilliams, James C. 1990. Isopycnal mixing in ocean circulation models. *J. Phys. Oceanogr.*, **20**(1), 150–155.
- Gent, Peter R, Willebrand, Jurgen, McDougall, Trevor J, & McWilliams, James C. 1995. Parameterizing eddy-induced tracer transports in ocean circulation models. *J. Phys. Oceanogr.*, **25**(4), 463–474.
- Griffies, SM. 2004. *Fundamentals of ocean climate models*.

- Isern-Fontanet, J. 2006. Vortices of the Mediterranean Sea: An altimetric perspective. *J. Phys.* ..., 87–103.
- Killworth, PD. 1998. Eddy parameterisation in large scale flow. *Ocean Model. Parameterization*.
- Killworth, Peter D., Chelton, Dudley B., & de Szoeke, Roland A. 1997. The Speed of Observed and Theoretical Long Extratropical Planetary Waves. *J. Phys. Oceanogr.*, 27(9), 1946–1966.
- Larichev, Vitaly D., & Held, Isaac M. 1995. Eddy amplitudes and fluxes in a homogeneous model of fully developed baroclinic instability. *J. Phys. Oceanogr.*, 25(10), 2285–2297.
- Le Traon, P-Y, & Minster, J-F. 1993. Sea level variability and semianual Rossby waves in the South Atlantic subtropical gyre. *J. Geophys. Res. Ocean.*, 98(C7), 12315–12326.
- Marshall, David P., & Adcroft, Alistair J. 2010. Parameterization of ocean eddies: Potential vorticity mixing, energetics and Arnold's first stability theorem. *Ocean Model.*, 32(3-4), 188–204.
- Marshall, JC. 1981. On the parameterization of geostrophic eddies in the ocean. *J. Phys. Oceanogr.*
- Matano, Ricardo P, Schlax, Michael G, & Chelton, Dudley B. 1993. Seasonal variability in the southwestern Atlantic. *J. Geophys. Res. Ocean.*, 98(C10), 18027–18035.
- Matsuura, Tomonori, & Yamagata, Toshio. 1982. On the evolution of nonlinear planetary eddies larger than the radius of deformation. *J. Phys. Oceanogr.*, 12(5), 440–456.
- Nof, Doron. 1981. On the β -induced movement of isolated baroclinic eddies. *J. Phys. Oceanogr.*, 11(12), 1662–1672.
- Oestreicher, Samantha. 2009. Underwater Mathematics : Illuminating Deep-Reaching Ocean Eddies in Climate Models.
- Okubo, Akira. 1970. Horizontal dispersion of floatable particles in the vicinity of velocity singularities such as convergences. *Deep sea Res. Oceanogr. Abstr.*, 17(143), 445–454.
- Olbers, Dirk, Willebrand, Jürgen, & Eden, Carsten. 2012. *Ocean Dynamics*. Springer.
- Rhines, Peter B. 1974. Waves and turbulence on a beta-plane. *J. Fluid Mech.*, 69(03), 417.
- Rhines, Peter B, & Holland, William R. 1979. A theoretical discussion of eddy-driven mean flows. *Dyn. Atmos. Ocean.*, 3(2), 289–325.

- Scott, Robert B, & Wang, Faming. 2005. Direct evidence of an oceanic inverse kinetic energy cascade from satellite altimetry. *J. Phys. Oceanogr.*, **35**(9), 1650–1666.
- Seibold, Benjamin. 2008. A compact and fast Matlab code solving the incompressible Navier-Stokes equations on rectangular domains mit18086 navierstokes . m Incompressible Navier-Stokes Equations. 1–16.
- Smith, K. Shafer, & Marshall, John. 2009. Evidence for Enhanced Eddy Mixing at Middepth in the Southern Ocean. *J. Phys. Oceanogr.*, **39**(1), 50–69.
- Treguier, AM. 1997. Parameterization of quasigeostrophic eddies in primitive equation ocean models. *J. Phys.* . . . , 567–580.
- Tulloch, Ross, Marshall, John, & Smith, K. Shafer. 2009. Interpretation of the propagation of surface altimetric observations in terms of planetary waves and geostrophic turbulence. *J. Geophys. Res.*, **114**(C2), C02005.
- Vollmer, Lukas, & Eden, Carsten. 2013. A global map of meso-scale eddy diffusivities based on linear stability analysis. *Ocean Model.*, **72**(Dec.), 198–209.
- Weiss, John. 1991. The dynamics of enstrophy transfer in two-dimensional hydrodynamics. *Physica*, **48**, 273–294.
- Zhang, Zhengguang, Zhang, Yu, Wang, Wei, & Huang, Rui Xin. 2013. Universal structure of mesoscale eddies in the ocean. *Geophys. Res. Lett.*, **40**(14), 3677–3681.

TODO: bibtex warnings

TODO: abc

TODO: units 2 siunits

TODO: flatten some complex pdfs

TODO: check overlaps of figs